Czech Technical University in Prague
Faculty of Electrical Engineering
Department of Physics

DESCRIPTION AND GENERATION OF LARGE-AMPLITUDE ACOUSTIC FIELDS IN CLOSED SPACES

Doctoral Thesis

MARTIN ŠOLTÉS

Prague, May 2015

Ph.D. Programme: Electrical Engineering and Information Technology
Branch of study: No. 2609V001 - Acoustics

SUPERVISOR: Doc. Dr. Ing. Michal Bednařík
SUPERVISOR - SPECIALIST: Ing. Milan Červenka Ph.D.

AFFIDAVIT

I hereby declare that this thesis has been written only by the undersigned and without any assistance from third parties.

Furthermore, I confirm that no sources have been used in the preparation of this thesis other than those indicated in the thesis itself.

ABSTRACT

Thesis deals with the problem of generation, description and utilisation of high-amplitude acoustic fields in closed cavities. A one dimensional, second-order partial differential model equation describing a sound field inside an axi-symmetrical variable-radius resonator is derived from basic fluid mechanics equations. Linearised model of the coupled loudspeaker-resonator acousto-mechanical system which includes the model of energy losses in the boundary layer due to turbulence is presented. A new evolution algorithm-based method for optimization of the acoustic-resonator shapes for generation of high-amplitude acoustic fields is presented. Numerical results show that use of a properly optimized resonant cavity results in substantially stronger acoustic field compared with simple-shaped resonators of similar dimensions. An acoustic compressor is built using the optimally-shaped acoustic resonator and a low-cost compression driver. It is shown that the performance of such a simple compressor is comparable or better than the acoustic compressors built previously by other researchers using non-optimally shaped resonators with more sophisticated driving mechanisms and valve arrangements.

ABSTRAKT

Dizertačná práca sa zaoberá problémom generovania, popisu a využitia extrémne silných zvukových polí v uzavretýh priestoroch. Jednorozmerná parciálna diferenciálna modelová rovnica druhého stupňa popisujúca zvukové pole v osovo symetrickom rezonátore premenlivého prierezu je odvodená zo základných rovníc mechaniky kontinua. Je prezentovaný linearizovaný model akusto-mechanického systému, ktorý zahrňuje turbulentné straty v okrajovej vrstve. Ďalej je predstavená nová metóda pre optimalizáciu tvaru akustického rezonátoru založená na evolučných algoritmoch. Numerické výsledky ukazujú, že v porovnaní s rezonátormi jednoduchých tvarov, použitie optimalizovaných rezonátorov umožňuje dosiahnuť výrazne silnejšie akustické polia. Akustický kompresor je zkonštruovaný použitím optimalizovaného rezonátoru a bežne dostupného kompresného tlakového reproduktoru. Je ukázané, že parametre takého kompresoru sú porovnateľné alebo lepšie ako parametre kompresorov postavených inými výskumníkmi používajúcimi neoptimalizované rezonátory s komplikovanejším budením a komplikovanejším systémom ventilov.

PUBLICATIONS

Publications in journals with impact factor

- Červenka M., Šoltés M., Bednařík M.: Optimal shaping of acoustic resonators for the generation of high-amplitude standing waves. The Journal of the Acoustical Society of America. 2014, vol. 136, no. 3, p. 1003-1012.
  Cited in: Xing Fan, Jun Chen, Jin Yang, Peng Bai, Zhaoling Li, and Zhong Lin Wang: Ultrathin, Rollable, Paper-Based Triboelectric Nanogenerator for Acoustic Energy Harvesting and Self-Powered Sound Recording. ACS Nano 2015 9 (4), 4236-4243

Publications in peer-reviewed journals and conference papers

- Červenka M., Bednařík M., Plocek J., Šoltés M.: Nízkofrekvenční zvukové svazky. Akustické listy. 2011, roč. 17, č. 4, s. 21-25.

- Šoltés M., Červenka M.: Simple Loudspeaker-driven Acoustic Compressor. Akustické listy. 2010, vol. 16, no. 4, p. 15-18.

- Šoltés M., Červenka M.: Optimization of Resonator Shape in a Coupled Loudspeaker-Resonator Acoustic System. In Euronoise Prague 2012 Proceedings. Prague: Czech Acoustic Society, 2012, p. 572-576.

- Šoltés M., Červenka M.: Acoustic compressor driven by horn loudspeaker. In Proceedings of Forum Acusticum 2011. Madrid: European Acoustics Association, 2011, p. 2837-2840.

"The stars are matter, We're matter, But it doesn't matter."

— *Cpt. Beefheart*

ACKNOWLEDGEMENTS

I would like to thank to my supervisors *Doc. Dr. Ing. Michal Bednařík* and *Ing. Milan Červenka Phd.* for the opportunity to work in the field of acoustics and also for their encouraging guidance.

I acknowledge support by the GACR grant P101/12/1925.

My thanks also belong to my family and friends for their love and support.

CONTENTS

LIST OF FIGURES

LIST OF TABLES

1

INTRODUCTION

1.1 LITERATURE

High amplitude standing waves in closed cavities have been studied extensively by many researchers. Much of the effort has been devoted to the study of finite amplitude standing waves in resonators driven at, or close to, one of its resonance modes. In order to achieve very high acoustic pressures, various powerful sources of excitation were used by researches (electrodynamic shakers were used by Lawrenson *et al.* [37] and Cruikshank [15], electromagnetic vibrators by Coppens and Sanders [14]). However, no matter how strong the excitation, the maximum acoustic pressure amplitudes obtained in the constant cross-section resonators were limited. It is now a well known fact that when resonators of cylindrical shape are excited at their resonant frequency, acoustic energy is transferred from the fundamental harmonic component to higher harmonics due to non-linear wave interactions. This leads to the distortion of the wave profile and eventually to the formation of shock. Because dissipation of acoustic energy is directly proportional to square of frequency, shock formation sets the upper limit for maximum acoustic pressure in such a resonator – the effect known as acoustic saturation. For practical purposes (e. g. acoustic compressors, stabilization of electric discharges for plasma-chemical reactors, thermoacoustic devices, acoustic mixers) this

is an undesirable effect and hence several techniques for achieving high pressure amplitudes have been proposed.

Gaitan and Atchley [20] showed that it is possible to prevent formation of shock waves in resonators with a variable cross-section, in which energy transfer from the fundamental harmonic component to the higher ones is significantly reduced. Major breakthrough in the field occurred in the year 1998 when Lawrenson *et al.* [37] published their experimental paper in which they introduced the concept of Resonant Macrosonic Synthesis (RMS). They showed that relative phases and amplitudes of the harmonics can be controlled by the resonator geometry resulting in shock-free waveforms of extremely high amplitudes. Acoustic pressure amplitudes, which they obtained, were more than an order higher than it had been possible before. Authors demonstrated a strong dependence of obtained maximum amplitudes on the resonator shapes (cylindrical, conical, horn-cone hybrid and bulb). Other methods for suppressing shock-wave formation involve using multiple Helmholtz's resonators tuned close to the second harmonics frequency arranged along the tube described by Sugimoto *et al.* [50], active feedback control where resonator is driven at two frequencies – the fundamental harmonic and second harmonic whose phase and gain are controlled by the feedback mechanism, see Huang *et al.* [27] or utilization of the parametric amplification [21] or selective absorbers [6].

Ilinskii *et al.* [30] presented in their theoretical paper a one-dimensional mathematical model equation expressed in terms of the velocity potential for description of high-amplitude standing waves in axi-symmetric, arbitrarily shaped acoustic resonators. The model includes nonlinearity, viscous bulk attenuation and entire-resonator driving by an external force (shaker-driving). They solved the model numerically in the frequency do-

main using the Runge-Kutta method. Numerical results were in good agreement with the experimental ones. The model was subsequently supplemented to account for energy losses in the boundary-layer and the losses due to acoustically generated turbulence, see Ilinskii *et al.* [31].

Chun and Kim [12] investigated numerically the influence of the shape of an entirely-driven resonator on the compression ratio (ratio of the maximum and minimum pressure attained at a chosen point in a resonator cavity during one period) using a quasi-one-dimensional model equation based on the conservation laws integrated in the time-domain using a high-order finite-difference scheme. From the several simple studied shapes (cylindrical, conical, 1/2-cosine and 3/4-cosine), the 1/2-cosine offered the best performance.

Erickson and Zinn [18] used an algorithm based on the modified Galerkin-method to solve the set of equations derived by Ilinsky *et al.* [30]. They also showed that in the exponentially shaped resonator the compression ratio strongly and non-trivially depends on its geometrical properties.

Luo *et al.* [39] studied theoretically the effect of the resonator shape on its compression ratio for the case of axi-symmetric, low-aspect-ratio exponential geometry. They found that the compression ratio decreases with shortening of the resonator length and smaller radius-to-length ratio.

Li *et al.* [38] presented a method for optimization of parameters of simple-shaped resonator cavities in order to maximize the compression ratio. They used numerical simulations based on a nonlinear wave equation with volume acoustic energy attenuation model.

Min *et al.* [43] conducted experiments, showing that it is possible to generate strongly nonlinear acoustic fields in loudspeaker-driven dissonant tubes.

Resonator shapes investigated in all of the papers mentioned above have one common feature: they were described by simple elementary functions and more general resonator shapes were not considered.

Červenka and Bednařík [54], Šoltés and Červenka [58] and Červenka *et al.* [55] used a more general approach of parameterizing acoustic resonator shapes using control points interconnected with cubic-splines.

With the progress in both theoretical description and experimental results in the field of high-amplitude acoustic fields a number of different practical applications emerged, e. g. acoustic compressors, plasma-chemical reactors [44], thermoacoustic devices [52], etc.

The possibility of constructing an acoustic compressor has been investigated by several authors (Bodine [8], Lucas [41], El-Sabbagh [16], Masuda and Kawashima [42] and Hossain *et al.* [26]). Acoustic compressors offer several advantages over the traditional ones. Most importantly they do not contain moving parts which require oils to reduce friction and wear – this is important in applications where mixing of oil with the compressed fluid is undesirable. Moving parts also reduce reliability of the compressor since they are subject to mechanical fatigue and failure. Another advantage is that acoustic compressors allow for a valveless construction [41].

1.2 PROBLEM STATEMENT

This thesis aims to present an Evolutionary algorithm-based optimization procedure for optimization of axi-symmetrical resonators based on linear theory which includes a model of dissipation of acoustic energy in the boundary layer. A method which allows to search in a much bigger space of more general resonator shapes then was possible before is proposed.

Loudspeaker driving was chosen as a means of introducing acoustic energy into the resonator since this is probably the most interesting case with respect to applications[1].

Proposed optimization method needs to be validated experimentally – resonator is manufactured and its performance is compared with the theory. Practical utilisation of high-amplitude acoustic fields made possible by the optimized resonator is experimentally demonstrated by the construction of a working example of a loudspeaker-driven acoustic compressor.

1.3 OVERVIEW OF THE THESIS

Thesis is divided into three parts. In the first part the model equation for description of standing waves in acoustic cavities is derived from the basic conservation laws and equation of state. The model is then presented in the form suitable for numerical calculations. Next, linearised model of the coupled loudspeaker-acoustic resonator system is presented in a form convenient for application in an optimization algorithm. Moreover, a model of acoustic energy dissipation in the boundary layer is incorporated into the linearised loudspeaker-acoustic resonator model. Finally, after a short review of different Evolutionary algorithms, an optimization procedure for resonator shape optimization based on the Evolutionary strategies is presented.

In the second part the loudspeaker-acoustic resonator system model developed in the first part is experimentally validated. Performance of the proposed optimization procedure is assessed and results of numerical

1 Proposed method can however work just as well with piston or entirely-driven resonators.

experiments are presented and confirmed experimentally. Finally, the possibility of the construction of a loudspeaker-driven acoustic compressor is demonstrated experimentally.

In the part III we conclude the thesis.

Details of the loudspeaker modelling are summarized in Appendix.

1.4 KEY THESIS CONTRIBUTIONS

Several novel ideas are proposed in the thesis. First of all an Evolutionary algorithm-based optimization procedure which searches the space of possible axi-symmetrical resonator shapes defined by n control-points evenly distributed along the resonator axis of symmetry[2] is presented. This is a major difference compared with the previously used methods which considered only resonator shapes given by elementary functions. Moreover, the focus is on the optimization of the loudspeaker-acoustic resonator system which was not considered before at all. Some of the results were already published in papers [55] and [58]. A different optimization constraints-handling method which was not published before is presented in the thesis.

Furthermore, the possibility of the construction of a loudspeaker driven acoustic compressor is demonstrated (again some of the experiments were already published in paper [57]).

2 Resonator shape is given by the cubic spline interpolation of the n control-points.

Part I

THEORETICAL PART

2

FLUID MECHANICS EQUATIONS

Throughout this text the description of the acoustic field is based on the theory of motion of a continuous fluid. Variables are described using Euler coordinates[1] in a Cartesian coordinate system. The state of the fluid at any point $\boldsymbol{r} = (x_1, x_2, x_3)$ and time t is given by six variables: three velocity components $\boldsymbol{v} = [(v_1(\boldsymbol{r}, t), v_2(\boldsymbol{r}, t), v_3(\boldsymbol{r}, t)]$ and three state variables: pressure $p(\boldsymbol{r}, t)$, density $\rho(\boldsymbol{r}, t)$ and temperature $\Theta(\boldsymbol{r}, t)$ and thus system of six equations describing the relationships between these variables are needed. Five of these equations are derived from the conservation theorems and the last equation is the state equation of the ideal gas[2]. By combining these equations, nonlinear model equation of large-amplitude acoustic fields can be derived.

2.1 CONTINUITY EQUATION

Continuity equation in fluid mechanics states that the mass is conserved during the fluid motion. More specifically, we say that the increase per time of the mass in a fixed arbitrary volume V is equal to the net influx of the fluid through the boundary S surrounding the volume V. Mathematically it is expressed as

1 Dependent variables are described in a fixed (but arbitrary) point.

2 We will be dealing with acoustic field in gases exclusively.

$$\oiint_S \rho v_i \nu_i \mathrm{d}S = -\frac{\mathrm{d}}{\mathrm{d}t} \iiint_V \rho \mathrm{d}V, \tag{2.1}$$

where $\boldsymbol{\nu} = (\nu_1, \nu_2, \nu_3)$ is a normal unit vector pointing outwards from the element area $\mathrm{d}S$ and $\rho v_i \nu_i \mathrm{d}S$ is a notation that uses Einstein summation convention

$$v_i \nu_i \equiv \sum_{k=1}^{3} v_i \nu_i. \tag{2.2}$$

Using Gauss's divergence theorem[3] we obtain

$$\iiint_V \left[\frac{\partial \rho}{\partial t} + \boldsymbol{\nabla} \cdot (\rho \boldsymbol{v}) \right] \mathrm{d}V = 0. \tag{2.3}$$

Since the volume V is chosen arbitrarily it follows that

$$\frac{\partial \rho}{\partial t} + \boldsymbol{\nabla} \cdot (\rho \boldsymbol{v}) = 0. \tag{2.4}$$

Using vector identity

$$\boldsymbol{\nabla} \cdot (a\boldsymbol{b}) = a \boldsymbol{\nabla} \cdot \boldsymbol{b} + (\boldsymbol{b} \cdot \boldsymbol{\nabla}) a,$$

Eq. (2.4) can be rewritten in the following form

$$\frac{\mathrm{D}\rho}{\mathrm{D}t} + \rho \boldsymbol{\nabla} \cdot \boldsymbol{v} = 0, \tag{2.5}$$

where operator $\mathrm{D}\cdot/\mathrm{D}t$ is a substantial time derivative expressed as

$$\frac{\mathrm{D}f}{\mathrm{D}t} = \frac{\partial f}{\partial t} + (\boldsymbol{v} \cdot \boldsymbol{\nabla}) f.$$

3 $\iiint_V \nabla \cdot \boldsymbol{F} \mathrm{d}V = \oiint_S \boldsymbol{F} \cdot \boldsymbol{n} \mathrm{d}S$

2.2 NAVIER-STOKES EQUATIONS

Navier-Stokes equations are mathematical expression of conservation of momentum theorem. It states that the increase per time of the momentum inside a fixed arbitrary volume V is equal to the net influx per time of the momentum inside the volume V plus the resultant of the outside forces acting on the volume V. Mathematically it is expressed as

$$\frac{\partial}{\partial t}\iiint\limits_V \rho v_i \mathrm{d}V = \iiint\limits_V \rho B_i \mathrm{d}V + \oiint\limits_S \sigma_{ik}\mathrm{d}S_k - \oiint\limits_S \rho v_i v_k \mathrm{d}S_k, \tag{2.6}$$

where σ_{ik} is the symmetric stress tensor and B_i is the volume force per unit mass. Vector $\mathbf{d}\boldsymbol{S}$ is defined as $\mathbf{d}\boldsymbol{S} = \boldsymbol{\nu}\mathrm{d}S$. Using Gauss' theorem, we obtain

$$\frac{\partial}{\partial t}\left(\rho v_i\right) = \rho B_i + \frac{\partial}{\partial x_k}\left(\sigma_{ik}\right) - \frac{\partial}{\partial x_k}\left(\rho v_i v_k\right). \tag{2.7}$$

Using Eq. (2.4) in Eq. (2.7) results in Newton's second law of motion

$$\rho\frac{\mathrm{D}v_i}{\mathrm{D}t} \equiv \rho\frac{\partial v_i}{\partial t} + \rho\frac{\partial v_i}{\partial x_k}v_k = \rho B_i + \frac{\partial}{\partial x_k}(\sigma_{ik}). \tag{2.8}$$

It can be shown (see e.g. [9], [17]) that for isotropic viscous fluid, the stress tensor σ_{ik} is expressed as

$$\sigma_{ik} = -p\delta_{ik} + \sigma'_{ik}, \tag{2.9}$$

where δ_{ik} is the Kronecker's delta[4]. First term on the right hand side of this equation says that force of the value p acts on any unit area immersed in fluid (ideal or viscous) and points in the opposite direction relative to

4 Kronecker's delta is a mathematical operator defined as $\delta_{ik} = 1$ when $i = k$ and $\delta_{ik} = 0$ when $i \neq k$.

the area's normal vector. The second term, σ'_{ik}, describes the resistance experienced by the particles against their relative motion in a viscous fluid. For ideal fluid

$$\sigma'_{ik} = 0 \tag{2.10}$$

and for viscous fluid, assuming the variation of the velocity field is small enough[5],

$$\sigma'_{ik} = \eta \left(\frac{\partial v_i}{\partial x_k} + \frac{\partial v_k}{\partial x_i} - \frac{2}{3}\delta_{ik}\frac{\partial v_r}{\partial x_r} \right) + \delta_{ik}\zeta \frac{\partial v_r}{\partial x_r}, \tag{2.11}$$

where η is the shear viscosity coefficient and ζ is the bulk viscosity coefficient and both are assumed to be constants. Inserting Eq. (2.9) into Eq. (2.7) we obtain the Navier-Stokes equations in the form

$$\rho \left(\frac{\partial v_i}{\partial t} + \frac{\partial v_i}{\partial x_k} v_k \right) = \rho B_i - \frac{\partial p}{\partial x_i} + \eta \frac{\partial^2 v_i}{\partial x_k \partial x_k} + \left(\zeta + \frac{\eta}{3} \right) \frac{\partial}{\partial x_i} \frac{\partial v_k}{\partial x_k}, \tag{2.12}$$

or in vector notation

$$\rho \left[\frac{\partial \boldsymbol{v}}{\partial t} + (\boldsymbol{v} \cdot \boldsymbol{\nabla})\, \boldsymbol{v} \right] = \boldsymbol{F} - \boldsymbol{\nabla} p + \eta \boldsymbol{\nabla}^2 \boldsymbol{v} + \left(\zeta + \frac{\eta}{3} \right) \boldsymbol{\nabla} \left(\boldsymbol{\nabla} \cdot \boldsymbol{v} \right), \tag{2.13}$$

where $\boldsymbol{F} = \rho \boldsymbol{B}$ is a force per volume. Using vector identity

$$\boldsymbol{\nabla}(\boldsymbol{\nabla} \cdot \boldsymbol{v}) = \boldsymbol{\nabla}^2 \boldsymbol{v} + \boldsymbol{\nabla} \times \boldsymbol{\nabla} \times \boldsymbol{v}$$

Eq. (2.13) can be rewritten in a more common form

$$\rho \left[\frac{\partial \boldsymbol{v}}{\partial t} + (\boldsymbol{v} \cdot \boldsymbol{\nabla}) \boldsymbol{v} \right] = \boldsymbol{F} - \boldsymbol{\nabla} p + \left(\zeta + \frac{4}{3}\eta \right) \boldsymbol{\nabla}^2 \boldsymbol{v} + \left(\zeta + \frac{\eta}{3} \right) \boldsymbol{\nabla} \times \boldsymbol{\nabla} \boldsymbol{v}. \tag{2.14}$$

5 Variation of the velocity field is described by the first derivative of the velocity with regard to spatial coordinates.

For the special case of inviscid flow, when $\zeta = \eta = 0$, Eq (2.13) turns into

$$\rho\left[\frac{\partial \boldsymbol{v}}{\partial t} + (\boldsymbol{v}\cdot\boldsymbol{\nabla})\boldsymbol{v}\right] - \boldsymbol{F} + \boldsymbol{\nabla}p = \boldsymbol{0}. \tag{2.15}$$

Eq. (2.15) together with the continuity Eq. (2.4) form a set of equations referred to as Euler's fundamental hydrodynamic equations.

2.3 CONSERVATION OF ENERGY

Conservation of energy law for fluid mechanics can be formulated in the following fashion: increase per time of the energy content inside the fixed arbitrary volume V surrounded by its boundary S is equal to the net influx per time of the energy inside the volume V through S due to the fluid motion, work per time done by the outside forces acting on the fluid in the volume V and the net influx per time of the heat inside the volume V through S. Mathematically it is expressed as

$$\frac{\partial}{\partial t}\iiint\limits_V \rho e \mathrm{d}V = -\oiint\limits_S \rho e v_i \mathrm{d}S_i + \oiint\limits_S v_i\sigma_{ik}\mathrm{d}S_k - \oiint\limits_S q_i \mathrm{d}S_i, \tag{2.16}$$

where e is the total energy per mass and $\boldsymbol{q}$ is the heat flow density. Using Gauss' divergence theorem and the fact that V is arbitrary, Eq. (2.16) can be rewritten as

$$\frac{\partial}{\partial t}(\rho e) + \frac{\partial}{\partial x_i}(\rho e v_i) + \frac{\partial q_i}{x_i} - \frac{\partial}{\partial x_k}(v_i\sigma_{ik}) = 0, \tag{2.17}$$

which is a differential form of the energy conservation theorem. Using Eq. (2.9), Eq (2.17) can be rewritten in the following form

$$\frac{\partial}{\partial t}(\rho e) + \frac{\partial}{\partial x_i}(\rho e v_i) + \frac{\partial q_i}{x_i} - \frac{\partial}{\partial x_i}(p v_i) + \frac{\partial \sigma'_{ik}}{\partial x_k} + \Phi, \tag{2.18}$$

where

$$\Phi \equiv \sigma'_{ik}\frac{\partial v_i}{\partial x_k} = \frac{1}{2}\eta\left(\frac{\partial v_i}{\partial x_k} + \frac{\partial v_k}{\partial x_i} - \frac{2}{3}\frac{\partial v_r}{\partial x_r}\delta_{ik}\right)^2 + \zeta\left(\frac{\partial v_k}{\partial x_k}\right)^2. \tag{2.19}$$

The total energy e is expressed as a sum of internal energy $e^{(i)}$ and mechanical energy $e^{(m)}$

$$e = e^{(i)} + e^{(m)}, \tag{2.20}$$

where mechanical energy $e^{(m)}$ is a sum of kinetic and potential energy. Multiplying Eq. (2.8) by v_i and assuming that B_i is conservative[6], we obtain

$$\rho v_i \frac{\mathrm{D}v_i}{\mathrm{D}t} = \rho v_i \frac{\partial \Phi}{\partial x_i} + v_i \frac{\partial \sigma_{ik}}{\partial x_k}, \tag{2.21}$$

or using continuity equation and Eq. (2.9) we get

$$\frac{\partial}{\partial t}\left(\frac{1}{2}\rho v^2 + \rho\Phi\right) + \frac{\partial}{\partial x_i}\left[\rho v_i\left(\frac{1}{2}v^2 + \Phi\right)\right] = v_i\frac{\partial \sigma'_{ik}}{\partial x_k} - v_i\frac{\partial p}{\partial x_i}, \tag{2.22}$$

where $v^2 = v_i v_i$. Assuming that

$$e^{(m)} = \Phi + \frac{1}{2}v^2 \tag{2.23}$$

and subtracting Eq. (2.22) from Eq. (2.18) results in

$$\frac{\partial}{\partial t}\left(\rho e^{(i)}\right) + \frac{\partial}{\partial x_k}\left(\rho e^{(i)} v_k\right) = -\frac{\partial q_k}{\partial x_k} - p\boldsymbol{\nabla}\cdot\boldsymbol{v} + \Phi. \tag{2.24}$$

For heat-conducting fluids, heat flow density vector $\boldsymbol{q}$ can be expressed, using Fourier's law, as

6 $\rho B_i = -\rho\frac{\partial \Phi}{\partial x_i}$

$$\boldsymbol{q} = -\kappa \boldsymbol{\nabla} \Theta, \tag{2.25}$$

where κ is the heat conduction coefficient and $\boldsymbol{\nabla}\Theta$ is the temperature gradient[7]. Combining the first and second law of thermodynamics yields the following well-known formula

$$\mathrm{d}e^{(i)} = \Theta \mathrm{d}s - p\mathrm{d}\left(\frac{1}{\rho}\right), \tag{2.26}$$

where s is entropy per mass. By substantial time derivation and using continuity equation, Eq. (2.26) is transformed into

$$\rho \frac{\mathrm{D}e^{(i)}}{\mathrm{D}t} = \rho\Theta \frac{\mathrm{D}s}{\mathrm{D}t} - p\boldsymbol{\nabla}\cdot\boldsymbol{v}. \tag{2.27}$$

Using continuity equation (2.4) it can be observed that the following formula holds for an arbitrary variable, for example for $u^{(i)}$ we have

$$\rho \frac{\mathrm{D}e^{(i)}}{\mathrm{D}t} = \frac{\partial}{\partial t}\left(\rho e^{(i)}\right) + \frac{\partial}{\partial x_k}\left(\rho e^{(i)} v_k\right). \tag{2.28}$$

Using Eq. (2.28) we can observe that the left-hand sides of equations (2.24) and (2.27) are equal. Putting the right-hand sides of these equation equal and using Fourier's law (2.25) and Eq. (2.19) results in the following form of the energy conservation theorem

$$\rho\Theta\left[\frac{\partial s}{\partial t} + (\boldsymbol{v}\cdot\boldsymbol{\nabla})\, s\right] = \kappa\boldsymbol{\nabla}^2\Theta + \zeta\left(\boldsymbol{\nabla}\cdot\boldsymbol{v}\right)^2 + \frac{1}{2}\eta\left(\frac{\partial v_i}{\partial x_k} + \frac{\partial v_k}{\partial x_i} - \frac{2}{3}\boldsymbol{\nabla}\cdot\boldsymbol{v}\delta_{ik}\right)^2. \tag{2.29}$$

In case the fluid is not heat-conducting ($\eta = 0$, $\zeta = 0$, $\kappa = 0$), Eq. (2.29) turns into

7 Equation holds for not-too-large temperature gradients. It is a first term of Taylor series expansion of the $\boldsymbol{q}(\Theta)$ function.

$$\left(\frac{\partial s}{\partial t} + v_k \frac{\partial}{\partial x_k}\right) = \frac{\mathrm{d}s}{\mathrm{d}t} = 0, \tag{2.30}$$

which suggests that under these circumstances the entropy is constant.

2.4 EQUATION OF STATE

State equation for an ideal gas describes the relationship between pressure, density and entropy per mass and can be derived from the first law of thermodynamics [9]. Lets start with the relation for a perfect (ideal) gas

$$\mathrm{d}e^{(i)} = c_V \mathrm{d}\Theta, \tag{2.31}$$

where c_V is the specific heat capacity of the fluid of constant volume. Combining (2.31) and (2.26) results in

$$\mathrm{d}s = c_V \frac{\mathrm{d}\Theta}{\Theta} + \frac{p}{\Theta}\mathrm{d}\left(\frac{1}{\rho}\right). \tag{2.32}$$

State equation of a perfect gas is expressed as

$$\frac{p}{\rho} = R\Theta, \tag{2.33}$$

where R is a gas constant. Taking the logarithm of this equation results in

$$\ln p + \ln \frac{1}{\rho} = \ln R + \ln \Theta. \tag{2.34}$$

By differentiating equation (2.34) following equation is obtained

$$\frac{\mathrm{d}p}{p} + \frac{\mathrm{d}v}{v} = \frac{\mathrm{d}\Theta}{\Theta}, \tag{2.35}$$

where $v = 1/\rho$ is the specific volume. Substituting equation (2.35) into (2.32) we get

$$\mathrm{d}s = c_V \left(\frac{\mathrm{d}p}{p} + \frac{\mathrm{d}v}{v} \right) + \frac{p}{\Theta} \mathrm{d}v. \tag{2.36}$$

Using (2.33) and rearranging, eqation (2.36) can be expressed as

$$\frac{\mathrm{d}s}{c_V} = \frac{\mathrm{d}p}{p} + \frac{c_V + R}{c_V} \frac{\mathrm{d}v}{v}. \tag{2.37}$$

Using Mayer's relation $R = c_p - c_V$, where c_p is the specific heat capacity of the fluid of constant pressure, equation (2.37) is further modified into

$$\frac{\mathrm{d}s}{c_V} = \frac{\mathrm{d}p}{p} + \gamma \frac{\mathrm{d}v}{v}, \tag{2.38}$$

where $\gamma = c_p/c_V$ is the ratio of specific heats. By integrating this equation we get

$$\frac{s - s_0}{c_V} = \ln \left[\left(\frac{p}{p_0} \right) \left(\frac{v}{v_0} \right)^{\gamma} \right]. \tag{2.39}$$

By taking into account that $v = 1/\rho$ and $v_0 = 1/\rho_0$ equation (2.39) can be rewritten in the following form

$$p = p_0 \left(\frac{\rho}{\rho_0} \right)^{\gamma} \mathrm{e}^{(s - s_0)/c_V}. \tag{2.40}$$

The change in entropy from its steady-state value due to acoustic wave is in most cases very small and therefore this equation can be further simplified, resulting in

$$p = p_0 \left(\frac{\rho}{\rho_0} \right)^{\gamma}. \tag{2.41}$$

However there are cases when entropy can not be considered to be constant. Some of these cases are

- Extremely large amplitude shock waves.
- When acoustic wave propagates in a heat-conducting medium, where entropy rises with the heat transfer.
- When numerous shock waves travel through the same area and temperature locally rises.

There is no known universally valid state equation. However it is possible to express the pressure as a function of the density and the entropy per mass using the Taylor expansion

$$p = p_0 + \left(\frac{\partial p}{\partial \rho}\right)_{s,\rho=\rho_0} (\rho - \rho_0) + \frac{1}{2}\left(\frac{\partial^2 p}{\partial \rho^2}\right)_{s,\rho=\rho_0} (\rho - \rho_0)^2 + \\ + \left(\frac{\partial p}{\partial s}\right)_{\rho,s=s_0} (s - s_0) + \left(\frac{\partial^2 p}{\partial \rho \partial s}\right)_{\rho=\rho_0,s=s_0} (\rho - \rho_0)(s - s_0) + ... \tag{2.42}$$

Omitting the last term, Eq. (2.42) can be rewritten in the following, frequently used form

$$p - p_0 \approx A\left(\frac{\rho - \rho_0}{\rho_0}\right) + \frac{B}{2}\left(\frac{\rho - \rho_0}{\rho_0}\right)^2 + \left(\frac{\partial p}{\partial s}\right)_{\rho,s=s_0} (s - s_0), \tag{2.43}$$

where

$$A = \rho_0 \left(\frac{\partial p}{\partial \rho}\right)_{s,\rho=\rho_0}, \tag{2.44}$$

$$B = \rho_0^2 \left(\frac{\partial^2 p}{\partial \rho^2}\right)_{s,\rho=\rho_0}. \tag{2.45}$$

For an ideal gas, coefficients A and B are expressed as

$$A = \rho_0 c_0^2, \tag{2.46}$$

$$B = \rho_0 c_0^2 (\gamma - 1), \tag{2.47}$$

where

$$c_0^2 = \left(\frac{\partial p}{\partial \rho}\right)_{s,\rho=\rho_0} = \frac{\gamma p_0}{\rho_0}. \tag{2.48}$$

c_0 is isentropic speed of sound. The ratio B/A, often called the parameter of nonlinearity, is a measure of the wave distortion. It can be expressed as

$$\frac{B}{A} = \frac{\rho_0}{c_0^2}\left(\frac{\partial^2 p}{\partial \rho^2}\right)_{s,\rho=\rho_0} = \frac{2\rho_0}{c_0}\left(\frac{\partial c}{\partial \rho}\right)_{s,\rho=\rho_0} = 2c_0\rho_0\left(\frac{\partial c}{\partial p}\right)_{s,p=p_0}, \tag{2.49}$$

where c is the speed of sound. Using Eq. (2.40) in Eq. (2.49), the parameter of nonlinearity for an ideal gas is obtained

$$\frac{B}{A} = \gamma - 1. \tag{2.50}$$

It can be shown (see e. g. [53]) that Eq. (2.43) can be further rewritten in the following form

$$p' = c_0^2 \rho' + \frac{c_0^2}{2\rho_0}(\gamma - 1)\rho'^2 - \kappa\left(\frac{1}{c_V} - \frac{1}{c_p}\right)\boldsymbol{\nabla}\cdot\boldsymbol{v}, \tag{2.51}$$

where $p' = p - p_0$ and $\rho' = \rho - \rho_0$.

2.5 SUMMARY OF THE BASIC EQUATIONS OF FLUID MECHANICS

Sound waves in non-viscous, heat non-conducting fluids are described by the system of Euler equations (Eq. (2.4), Eq. (2.15) and a state equation):

$$\frac{\partial \rho}{\partial t} + \boldsymbol{\nabla} \cdot (\rho \boldsymbol{v}) = 0, \tag{2.52a}$$

$$\rho \left[\frac{\partial \boldsymbol{v}}{\partial t} + (\boldsymbol{v} \cdot \boldsymbol{\nabla})\, \boldsymbol{v} \right] = \boldsymbol{F} - \boldsymbol{\nabla} p, \tag{2.52b}$$

$$p = p(\rho). \tag{2.52c}$$

Viscous, heat-conducting fluids are described by the following system of equations (Eq. (2.4), Eq. (2.14), Eq. (2.29) and a state equation):

$$\frac{\partial \rho}{\partial t} + \boldsymbol{\nabla} \cdot (\rho \boldsymbol{v}) = 0, \tag{2.53a}$$

$$\rho \left[\frac{\partial \boldsymbol{v}}{\partial t} + (\boldsymbol{v} \cdot \boldsymbol{\nabla}) \boldsymbol{v} \right] = \boldsymbol{F} - \boldsymbol{\nabla} p + \left(\zeta + \frac{4}{3} \eta \right) \boldsymbol{\nabla}^2 \boldsymbol{v} + \left(\zeta + \frac{\eta}{3} \right) \boldsymbol{\nabla} \times \boldsymbol{\nabla} \boldsymbol{v}, \tag{2.53b}$$

$$\rho \Theta \frac{\mathrm{D}s}{\mathrm{D}t} = \kappa \boldsymbol{\nabla}^2 \Theta + \zeta \left(\boldsymbol{\nabla} \cdot \boldsymbol{v} \right)^2 + \frac{1}{2} \eta \left(\frac{\partial v_i}{\partial x_k} + \frac{\partial v_k}{\partial x_i} - \frac{2}{3} \boldsymbol{\nabla} \cdot \boldsymbol{v} \delta_{ik} \right)^2, \tag{2.53c}$$

$$p = p(\rho, s). \tag{2.53d}$$

This system of equations is valid for nonlinear sound waver in viscous, heat-conductive, homogeneous fluids in which quantities η, ζ and κ are constant. In the case of heat-conducting gas, the state equation assumes the form given in Eq. (2.51).

3

DESCRIPTION OF THE NONLINEAR STANDING WAVES IN ACOUSTICAL RESONATORS

In the following chapter the model equation for the axisymmetrical resonator of variable cross-section will be derived from the basic equations of fluid mechanics presented in the previous chapter. Example of the axisymmetrical resonator, with radius $r(x)$ is shown in Fig. 1. It is assumed that $r(x) \ll \lambda$, where λ is the wavelength, so that transverse modes are not excited and only planar waves propagate inside the resonator. In this situation acoustical quantities are function of only one spatial coordinate x and a time t.

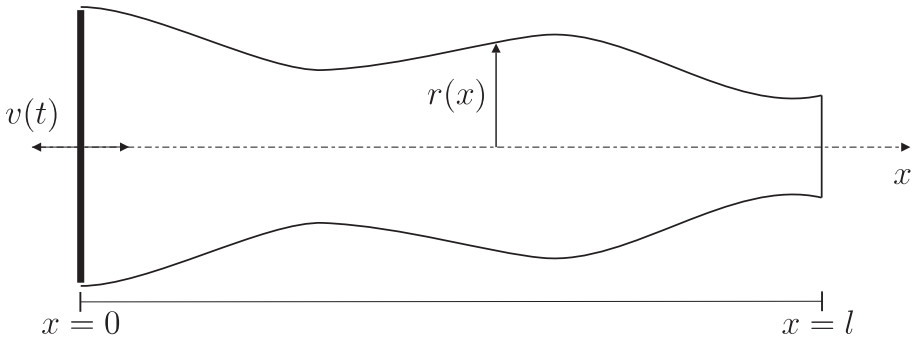

Figure 1: Cross-sectional view of the variable cross-section resonator.

3.1 FLUID MECHANICS EQUATIONS IN 1-D

For deriving one-dimensional model equations that describe nonlinear standing waves in resonators basic fluid mechanics equations need to be altered.

One-dimensional continuity equation for axisymmetric resonator can be expressed as [30]

$$\frac{\partial M_D}{\partial t} + \frac{\partial M_T}{\partial x} = 0, \tag{3.1}$$

where M_D is a fluid mass per unit length and M_T is a fluid mass flux through the resonator cross section of the radius r. They can be expressed as

$$M_D = \rho \pi r^2, \tag{3.2a}$$

$$M_T = \rho v \pi r^2. \tag{3.2b}$$

Substituting Eq. (3.2a) and (3.2b) into Eq. (3.1) results in

$$\frac{\partial \rho}{\partial t} + \frac{1}{r^2}\frac{\partial}{\partial x}\left(r^2 \rho v\right) = 0. \tag{3.3}$$

In case of constant-radius resonator, Eq. (3.3) reduces to

$$\frac{\partial \rho}{\partial t} + \frac{\partial}{\partial x}\left(\rho v\right) = 0. \tag{3.4}$$

By comparing Eq. (2.4) with Eq. (3.3) we find that divergence operator $\boldsymbol{\nabla}\cdot$ is in one dimension expressed as

$$\boldsymbol{\nabla} \cdot A = \frac{1}{r^2}\frac{\partial}{\partial x}\left(r^2 A\right). \tag{3.5}$$

Using Eq. (3.5), momentum equation Eq. (2.14) can be rewritten for variable-radius resonator in one-dimensional form

$$\frac{\partial v}{\partial t} + v\frac{\partial v}{\partial x} = F - \frac{1}{\rho}\frac{\partial p}{\partial x} + \frac{\zeta + 4\eta/3}{\rho}\frac{\partial}{\partial x}\left[\frac{1}{r^2}\frac{\partial}{\partial x}\left(r^2 v\right)\right], \tag{3.6}$$

where F is a x-component of the volume forces vector per unit volume. For constant-radius resonator, this equation reduces to

$$\frac{\partial v}{\partial t} + v\frac{\partial v}{\partial x} = F - \frac{1}{\rho}\frac{\partial p}{\partial x} + \frac{\zeta + 4\eta/3}{\rho}\frac{\partial^2 v}{\partial x^2}. \tag{3.7}$$

Finally the 1-D state equation (2.51) for the ideal gas-filled variable-radius resonator

$$p' = c_0^2\rho' + \frac{c_0^2}{2\rho_0}\left(\gamma - 1\right)\rho'^2 - \kappa\left(\frac{1}{c_V} - \frac{1}{c_p}\right)\frac{1}{r^2}\frac{\partial}{\partial x}\left(r^2 v\right) \tag{3.8}$$

and for the constant-radius resonator

$$p' = c_0^2\rho' + \frac{c_0^2}{2\rho_0}\left(\gamma - 1\right)\rho'^2 - \kappa\left(\frac{1}{c_V} - \frac{1}{c_p}\right)\frac{\partial v}{\partial x}. \tag{3.9}$$

3.2 BOUNDARY LAYER

When viscous fluid moves along the wall of the resonator tube, viscous forces cause molecules of the fluid to stick to the wall surface and hence the component of the acoustic velocity parallel with the wall surface tends to zero. Thin layer near the wall surface where an acoustic velocity rapidly changes is called a boundary layer. It is assumed that movement in the boundary layer has only a very small impact on the fluid outside the boundary layer and that it is sufficient to use linearised equations to describe small disturbances in the boundary layer [31]. Under these assumptions, the continuity equation for the one-dimensional flow in axisymmetric resonator with variable radius accounting for the boundary layer effects can be expressed as [31]

$$\frac{\partial \rho}{\partial t} + \frac{1}{r^2}\frac{\partial}{\partial x}\left(r^2 \rho v\right) = \frac{2\epsilon\rho}{r^2}\frac{\partial\left(\partial^{-1/2}\left(rv\right)\right)}{\partial x \partial t^{-1/2}}, \tag{3.10}$$

where

$$\epsilon = \sqrt{\nu}\left(1 + \frac{\gamma - 1}{\sqrt{Pr}}\right) \tag{3.11}$$

is a coefficient accounting for boundary-layer effects. $\nu = \eta/\rho_0$ is the kinematic viscosity and

$$Pr = \frac{\eta c_p}{\kappa} \tag{3.12}$$

is the Prandtl number. The minus-half-order partial derivative with respect to time is defined using the following integro-differential operator [49]

$$\frac{\partial^{-1/2} f\left(t, x\right)}{\partial t^{-1/2}} = \frac{1}{\sqrt{\pi}}\int_{-\infty}^{t} \frac{f\left(\tau, x\right)}{\sqrt{t - \tau}} \mathrm{d}\tau. \tag{3.13}$$

3.3 MODEL EQUATION FOR THE GAS-FILLED AXISYMMETRIC RESONATOR WITH VARIABLE RADIUS

For derivation of the model equation it is assumed that the fluid inside the resonator is subject to the outside volume forces, thanks to which the resonator cavity is moving with the acceleration $a(t)$. Volume force per unit volume can be expressed as

$$F = -\rho a\left(t\right). \tag{3.14}$$

Acoustic quantities are assumed to be small

$$\frac{|p-p_0|}{p_0} = \frac{|p'|}{p_0} \sim \mu, \qquad \frac{|\rho-\rho_0|}{\rho_0} = \frac{|\rho'|}{\rho_0} \sim \mu, \qquad \frac{|v|}{c_0} \sim \mu,$$

where μ is a small dimensionless parameter, p_0 is the barometric pressure and p_0 is the uniform density. Also it is assumed that the material parameters η, ζ, $\kappa \sim \mu$ and $|a| \sim \mu^2$.

We limit ourselves to the second-order approximation so terms in the respective equations of the third order and higher can be discarded and first-order approximations are substituted in the second-order terms producing error of the μ^3 order. Regarding the derivation that follows it is convenient to introduce a velocity potential function φ as

$$v = \frac{\partial \varphi}{\partial x}. \tag{3.15}$$

In the first approximation the state equation (3.8) reduces to

$$\rho' = \frac{p'}{c_0^2} \tag{3.16}$$

and the momentum equation (3.6) reduces to

$$\rho_0 \frac{\partial v}{\partial t} = -\frac{\partial p}{\partial x} - \rho_0 a. \tag{3.17}$$

Integrating this equation with respect to the spatial coordinate x and introducing velocity potential leads to

$$p = -\rho_0 \frac{\partial \varphi}{\partial t} - \rho_0 a x + p_0, \tag{3.18}$$

where p_0 is an integration constant. Acoustic pressure $p' = p - p_0$ is then expressed as

$$p' = -\rho_0 \frac{\partial \varphi}{\partial t} - \rho_0 a x \tag{3.19}$$

and using Eq. (3.16), equation for acoustic density is obtained

$$\rho' = -\frac{\rho_0}{c_0^2}\left(\frac{\partial\varphi}{\partial t} + ax\right). \tag{3.20}$$

Spatial derivatives can be eliminated by substituting the linear Webster's equation [7]

$$\frac{1}{r^2}\frac{\partial}{\partial x}\left(r^2\frac{\partial\varphi}{\partial x}\right) = \frac{1}{c_0}\frac{\partial^2\varphi}{\partial t^2} \tag{3.21}$$

into the second-order terms. Dropping third-order terms in momentum equation (3.6), introducing velocity potential, substituting for acoustic density from Eq. (3.20), using Eq. (3.21) in one of the second-order terms and integrating with respect to the spatial coordinate x results in

$$\begin{aligned} p' = -\rho_0\frac{\partial\varphi}{\partial t} - \rho_0 ax + \frac{\rho_0}{2c_0^2}\left(\frac{\partial\varphi}{\partial t}\right)^2 - \\ \frac{\rho_0}{2}\left(\frac{\partial\varphi}{\partial x}\right)^2 + \frac{1}{c_0^2}\left(\zeta + \frac{4}{3}\eta\right)\frac{\partial^2\varphi}{\partial t^2}. \end{aligned} \tag{3.22}$$

In similar manner, dropping third-order terms in continuity equation (3.10), using velocity potential function and employing Eq. (3.16), Eq. (3.19) and Eq. (3.21) in the second-order terms yields

$$\begin{aligned} \frac{\partial\rho'}{\partial t} = -\frac{\rho_0}{r^2}\frac{\partial}{\partial x}\left(r^2\frac{\partial\varphi}{\partial x}\right) + \frac{\rho_0}{2c_0^4}\frac{\partial}{\partial t}\left(\frac{\partial\varphi}{\partial t}\right)^2 + \\ + \frac{\rho_0}{2c_0^2}\frac{\partial}{\partial t}\left(\frac{\partial\varphi}{\partial x}\right)^2 + \frac{2\epsilon\rho_0}{r^2}\frac{\partial^{1/2}}{\partial x\partial t^{-1/2}}\left(r\frac{\partial\varphi}{\partial x}\right). \end{aligned} \tag{3.23}$$

Differentiating Eq. (3.8) with respect to time, introducing velocity potential and employing Eq. (3.16), Eq. (3.19) and Eq. (3.21) in the second-order terms yields

$$\frac{\partial p'}{\partial t} = c_0^2\frac{\partial\rho'}{\partial t} + \frac{\rho_0}{2c_0^2}(\gamma - 1)\frac{\partial}{\partial t}\left(\frac{\partial\varphi}{\partial t}\right)^2 - \frac{\kappa}{c_0^2}\left(\frac{1}{c_V} - \frac{1}{c_p}\right)\frac{\partial^3\varphi}{\partial t}. \tag{3.24}$$

Finally, differentiating Eq. (3.22) with respect to time and using Eq. (3.23) and Eq. (3.24) to eliminate acoustic pressure and acoustic density results in

$$\frac{\partial^2\varphi}{\partial t^2} - \frac{c_0^2}{r^2}\frac{\partial}{\partial x}\left(r^2\frac{\partial\varphi}{\partial x}\right) + \frac{\partial}{\partial t}\left(\frac{\partial\varphi}{\partial x}\right)^2 + \frac{\gamma-1}{2c_0^2}\frac{\partial}{\partial t}\left(\frac{\partial\varphi}{\partial t}\right)^2 + \\ + x\frac{\mathrm{d}a}{\mathrm{d}t} - \frac{\delta}{c_0^2}\frac{\partial^3\varphi}{\partial t^3} + \frac{2c_0\epsilon}{r^2}\frac{\partial^{1/2}}{\partial x\partial t^{-1/2}}\left(r\frac{\partial\varphi}{\partial x}\right) = 0, \qquad (3.25)$$

where

$$\delta = \frac{1}{\rho_0}\left[\zeta + \frac{4}{3}\eta + \kappa\left(\frac{1}{c_V} - \frac{1}{c_p}\right)\right] \qquad (3.26)$$

is the diffusivity of sound.

Equation (3.25) is a second-order model equation describing a sound field inside an axisymmetrical variable-radius resonator of arbitrary shape that is moving (shaking) along its axis with acceleration a. The equation takes into account viscosity and boundary-layer effects. For a resonator which is not moving[1] this equation reduces to

$$\frac{\partial^2\varphi}{\partial t^2} - \frac{c_0^2}{r^2}\frac{\partial}{\partial x}\left(r^2\frac{\partial\varphi}{\partial x}\right) + \frac{\partial}{\partial t}\left(\frac{\partial\varphi}{\partial x}\right)^2 + \frac{\gamma-1}{2c_0^2}\frac{\partial}{\partial t}\left(\frac{\partial\varphi}{\partial t}\right)^2 - \\ - \frac{\delta}{c_0^2}\frac{\partial^3\varphi}{\partial t^3} + \frac{2c_0\epsilon}{r^2}\frac{\partial^{1/2}}{\partial x\partial t^{-1/2}}\left(r\frac{\partial\varphi}{\partial x}\right) = 0. \qquad (3.27)$$

1 Sound field excitation can be included in the boundary condition.

4

NUMERICAL SOLUTION OF THE MODEL EQUATION

Since there is no known analytical solution to the Eq. (3.25) it has to be solved numerically. For the purpose of numerical computation it is convenient to introduce dimensionless variables, e. g. in the form

$$X = \frac{x}{l_r}, \quad R = \frac{r}{l_r}, \quad \Phi = \frac{\hat{\varphi}}{l_r^2 \omega_0}, \quad \Omega = \frac{\omega}{\omega_0},$$
$$V = \frac{\hat{v}}{\pi c_0}, \quad P = \frac{\hat{p}'}{\pi^2 \rho_0 c_0^2}, \quad A = \frac{a}{l_r \omega_0^2}, \quad T = \omega t, \tag{4.1}$$

where l_r is the total resonator length, $\omega = 2\pi f$ is the angular frequency of the resonator excitation, f is the frequency and ω_0 is the first eigenfrequency of a cylindrical resonator of the length l_r, given by the equation

$$\omega_0 = \frac{\pi c_0}{l_r}. \tag{4.2}$$

Using these dimensionless variables, Eq. (3.25) is transformed into

$$\frac{\partial}{\partial X}\left(R^2 \frac{\partial \Phi}{\partial X}\right) - \pi^2 \Omega^2 R^2 \frac{\partial^2 \Phi}{\partial T^2} - \pi^2 \Omega R^2 \frac{\partial}{\partial T}\left(\frac{\partial \Phi}{\partial X}\right)^2 -$$
$$-\pi^4 \Omega^3 \frac{\gamma - 1}{2} R^2 \frac{\partial}{\partial T}\left(\frac{\partial \Phi}{\partial T}\right)^2 - \pi^2 \Omega R^2 X \frac{\mathrm{d}A}{\mathrm{d}T} +$$
$$+\pi G \Omega^3 R^2 \frac{\partial^3 \Phi}{\partial T^3} - \frac{\Gamma}{\sqrt{\Omega}} \frac{\partial^{1/2}}{\partial^{-1/2} \partial X}\left(R \frac{\partial \Phi}{\partial X}\right) = 0, \tag{4.3}$$

where

$$G = \frac{\pi\omega_0\delta}{c_0^2} \tag{4.4}$$

is a coefficient accounting for thermoviscous and volume dissipation and

$$\Gamma = \frac{2\epsilon}{\sqrt{\pi c_0 l_r}} \tag{4.5}$$

is a coefficient accounting for boundary layer losses.

Eq. (4.3) can be rewritten into the set of two equations of the first–order with respect to the spatial derivatives

$$\frac{\partial\Phi}{\partial X} = \frac{W}{R^2}, \tag{4.6a}$$

$$\begin{aligned}\frac{\partial W}{\partial X} =& \pi^2\Omega^2 R^2\frac{\partial^2\Phi}{\partial T^2} + \frac{\pi^2\Omega}{R^2}\frac{\partial W^2}{\partial T} + \\ &+ \pi^4\Omega^3\frac{\gamma-1}{2}R^2\frac{\partial}{\partial T}\left(\frac{\partial\Phi}{\partial T}\right)^2 + \pi^2\Omega R^2 X\frac{\mathrm{d}A}{\mathrm{d}T} - \\ &- \pi G\Omega^3 R^2\frac{\partial^3\Phi}{\partial T^3} + \frac{\Gamma}{\sqrt{\Omega}}\frac{\partial^{-1/2}}{\partial T^{-1/2}}\left(\frac{1}{R}\frac{\partial W}{\partial X} - \frac{1}{R^2}\frac{\mathrm{d}R}{\mathrm{d}X}W\right).\end{aligned} \tag{4.6b}$$

Dimensionless acoustic pressure P and acoustic velocity V are then calculated using the following formulas (from Eq. (3.22))

$$P = -\Omega\frac{\partial\Phi}{\partial T} + \frac{\pi^2\Omega^2}{2}\left(\frac{\partial\Phi}{\partial T}\right)^2 - \frac{W^2}{2R^4} - AX + \frac{G'\Omega^2}{\pi}\frac{\partial^2\Phi}{\partial T^2}, \tag{4.7}$$

$$V = \frac{W}{R^2}, \tag{4.8}$$

where

$$G' = \frac{\pi\omega_0}{\rho_0 c_0^2}\left(\zeta + \frac{4}{3}\eta\right). \tag{4.9}$$

Resonator excitation is assumed to be periodic and dimensionless acceleration A in Eqs. (4.6) can be expressed by means of the complex Fourier series

$$A(T) = \sum_{k=-\infty}^{\infty} A_k \mathrm{e}^{\mathrm{i}kT}, \tag{4.10}$$

where i is the imaginary unit defined as $\mathrm{i} = \sqrt{-1}$. Because acceleration A is a real–valued function of time, it follows that $A_{-k} = A_k^*$, where symbol * signifies complex conjugate.

Because resonator excitation is assumed to be periodic, solution of the Eqs. (4.6) can also be expressed using Fourier series

$$\Phi(X,T) = \sum_{k=-\infty}^{\infty} \Phi_k \mathrm{e}^{\mathrm{i}kT}, \quad W(X,T) = \sum_{k=-\infty}^{\infty} W_k \mathrm{e}^{\mathrm{i}kT} \tag{4.11}$$

and again $\Phi_{-k} = \Phi_k^*$ and $W_{-k} = W_k^*$, with Φ_0 and W_0 being real-valued coefficients.

Derivatives of the function $F(X,T)$ expressed using Fourier series are given by the following formulas

$$\frac{\partial F}{\partial T} = \sum_{k=-\infty}^{\infty} \mathrm{i}kF_k \mathrm{e}^{\mathrm{i}kT}, \qquad \frac{\partial F}{\partial X} = \sum_{k=-\infty}^{\infty} \frac{\mathrm{d}F_k}{\mathrm{d}X} \mathrm{e}^{\mathrm{i}kT},$$
$$\frac{\partial^2 F}{\partial T^2} = \sum_{k=-\infty}^{\infty} -k^2 F_k \mathrm{e}^{\mathrm{i}kT}, \qquad \frac{\partial^2 F}{\partial X^2} = \sum_{k=-\infty}^{\infty} \frac{\mathrm{d}^2 F_k}{\mathrm{d}X^2} \mathrm{e}^{\mathrm{i}kT}.$$

Multiplication of the functions $F(X,T)$ and $G(X,T)$ is given by

$$FG = \sum_{k=-\infty}^{\infty} \sum_{j=-\infty}^{\infty} F_k G_j \mathrm{e}^{\mathrm{i}(k+j)T} = \sum_{k=-\infty}^{\infty} \sum_{m=-\infty}^{\infty} F_k G_{k-m} \mathrm{e}^{\mathrm{i}kT}, \tag{4.12}$$

where $m = k + j$.

For the purpose of numerical computation the number of harmonic components in the Fourier series has to be finite and therefore acoustic quantities are approximated using the following formulas

$$A = \sum_{k=-N}^{N} A_k \mathrm{e}^{\mathrm{i}kT}, \quad \Phi = \sum_{k=-N}^{N} \Phi_k \mathrm{e}^{\mathrm{i}kT}, \quad W = \sum_{k=-N}^{N} W_k \mathrm{e}^{\mathrm{i}kT}, \quad (4.13)$$

where N is the number of harmonic components used for the computation. k-th Fourier component of the multiplication of the functions F and G can be expressed as

$$[FG]_k = \sum_{m=-N+k}^{N} F_m G_{k-m}, \quad (4.14)$$

for $0 \leq k \leq N$. And again $[FG]_{-k} = [FG]_k^*$. Substituting Fourier series expressions into Eqs. (4.6) a system of ordinary differential equations is obtained in the following form

$$\frac{\mathrm{d}\Phi_k}{\mathrm{d}X} = \frac{W_k}{R^2}, \quad (4.15a)$$

$$\left(1 - \frac{\Gamma}{\sqrt{\mathrm{i}k\Omega}R}\right)\frac{\mathrm{d}W_k}{\mathrm{d}X} = -k^2\pi^2\Omega^2R^2\Phi_k + \mathrm{i}k\frac{\pi^2\Omega}{R^2}\sum_{j=k-N}^{N} W_{k-j}W_j - \\ -\mathrm{i}k\pi^4\Omega^3\frac{\gamma-1}{2}R^2\sum_{j=k-N}^{N}(k-j)\,j\Phi_{k-j}\Phi_j + \mathrm{i}k\pi^2\Omega R^2 X A_k + \\ +\mathrm{i}k^3\pi G\Omega^3R^2\Phi_k - \frac{\Gamma}{\sqrt{\mathrm{i}k\Omega}R^2}\frac{\mathrm{d}R}{\mathrm{d}X}W_k. \quad (4.15b)$$

This system of ordinary differential equations can be solved using e. g. fifth-order Runge-Kutta method [45] with boundary conditions given by

$$W_k = 0 \quad (4.16)$$

for $X = 0$ and $X = 1$.

Finally, Fourier components of the dimensionless acoustic pressure and acoustic velocity are expressed as

$$P_k = -\mathrm{i}k\Omega\Phi_k - \frac{\pi^2\Omega^2}{2}\sum_{j=k-N}^{N}(k-j)\,j\Phi_{k-j}\Phi_j - \frac{1}{2R^4}\sum_{j=k-N}^{N}W_{k-j}W_j - \\ - XA_k - \frac{k^2\Omega^2 G}{\pi}\Phi_k, \tag{4.17a}$$

$$V_k = \frac{W_k}{R^2}. \tag{4.17b}$$

5

LINEARISED MODEL OF THE LOUDSPEAKER-ACOUSTIC RESONATOR SYSTEM

5.1 LINEARISED ACOUSTIC RESONATOR MODEL

Sound field inside the axisymmetrical resonator in the first-order approximation can be obtained by dropping second-order terms in Eq. (3.27) which results in the following equation

$$\frac{\partial^2\varphi}{\partial t^2} - \frac{c_0^2}{r^2}\frac{\partial}{\partial x}\left(r^2\frac{\partial\varphi}{\partial x}\right) - \frac{\delta}{c_0^2}\frac{\partial^3\varphi}{\partial t^3} + \frac{2c_0^2\varepsilon}{r^2}\frac{\partial^{1/2}}{\partial x\partial t^{-1/2}}\left(r\frac{\partial\varphi}{\partial x}\right) = 0, \quad (5.1)$$

which is a 1-D linear equation describing axisymmetrical, variable cross-section, rigid-walled resonator in which thermo-viscous bulk attenuation and boundary layer attenuation are accounted for.

Assuming steady-state harmonically varying sound field, acoustic quantities can be expressed as

$$g(x,t) = \Re\left[\hat{g}(x)\, e^{\mathrm{i}\omega t}\right]. \quad (5.2)$$

Substituting this formula in Eq. (5.1) results in

$$\left(1 - \frac{2\epsilon}{\sqrt{\mathrm{i}\omega}r}\right)\frac{\mathrm{d}}{\mathrm{d}x}\left(r^2\frac{\mathrm{d}\hat{\varphi}}{\mathrm{d}x}\right) + \frac{2\epsilon}{\sqrt{\mathrm{i}\omega}}\frac{\mathrm{d}r}{\mathrm{d}x}\frac{\mathrm{d}\hat{\varphi}}{\mathrm{d}x} + \frac{\omega^2}{c_0^2}\left(1 - \frac{\mathrm{i}\omega\delta}{c_0^2}\right)r^2\hat{\varphi} = 0. \quad (5.3)$$

Assuming the resonator is driven by the electrodynamic loudspeaker attached at $x = l_r$, where l_r is the total length of the resonator and

terminated by the rigid wall at $x = 0$, the boundary conditions are the following

$$\mathcal{L}\left[\hat{p}'\left(x = l_r\right), \hat{v}\left(x = l_r\right), \hat{u}\right] = 0, \tag{5.4a}$$

$$\left.\frac{\mathrm{d}\hat{\varphi}}{\mathrm{d}x}\right|_{x=0} = 0, \tag{5.4b}$$

where $\mathcal{L}$ is a linear function of an acoustic pressure phasor $\hat{p}'$, an acoustic velocity phasor $\hat{v}$ and a driving voltage phasor $\hat{u}$ modeling the louspeaker driver. Since there is no known analytical solution to the Eq. (5.3) for a general $r(x)$, it has to be solved numerically. For this purpose it is convenient to introduce dimensionless variables in the form given in Eqs. (4.1). Using these variables, Eq. (5.3) can be expressed as

$$\frac{\mathrm{d}\Phi}{\mathrm{d}X} = \frac{W}{R^2}, \tag{5.5a}$$

$$\left(1 - \frac{\Gamma}{\sqrt{\mathrm{i}\Omega}}\right)\frac{\mathrm{d}W}{\mathrm{d}X} = -\pi^2\Omega^2 R^2\left(1 - \frac{\mathrm{i}G\Omega}{\pi}\right)\Phi - \frac{\Gamma}{\sqrt{\mathrm{i}\Omega}R^2}\frac{\mathrm{d}R}{\mathrm{d}X}W. \tag{5.5b}$$

Equations (5.5) form a system of four linear first-order ordinary differential equations for real and imaginary parts of Φ and W variables. These equations can be integrated numerically using e. g. fifth-order Runge-Kutta method [45]. Boundary value problem can be solved using e. g. the shooting method [45]. Dimensionless acoustic pressure and acoustic velocity are calculated using the following equations

$$P = -\mathrm{i}\Omega\Phi - \frac{\Omega^2 G'}{\pi}\Phi, \tag{5.6a}$$

$$V = \frac{W}{R^2}. \tag{5.6b}$$

5.2 LOUDSPEAKER

A loudspeaker is an electrodynamic type which can be modelled using equivalent lumped-element circuit [56] shown in Fig. 2.

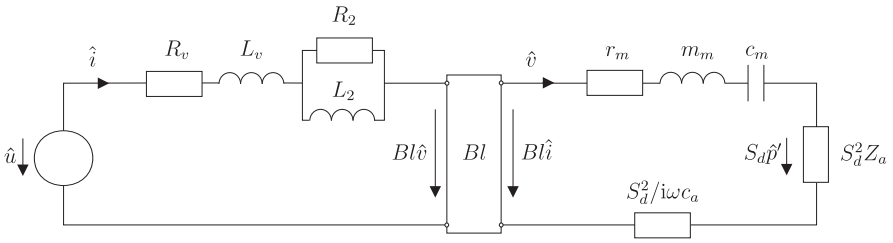

Figure 2: Lumped-element circuit of an electrodynamic loudspeaker.

Meaning of the symbols in Fig. 2 is the following: $\hat{u}$ is the phasor of the input voltage present on the loudspeaker terminals, $\hat{i}$ is the phasor of the electric current, $\hat{v}$ is the phasor of the velocity, $\hat{p}'$ is the phasor of the acoustic pressure, B is the magnetic field strength in the magnet air gap, l is the length of the voice coil wire, S_d is the diaphragm area,

$$c_a = \frac{V}{\rho_0 c_0^2} \tag{5.7}$$

is the compliance of the air enclosed behind the diaphragm in the volume V. Meaning of the rest of the symbols is clear from Table 1.

R_2 and L_2 are significant only at high frequencies [32] and therefore will be neglected in further derivation. The relationship between input voltage $\hat{u}$, velocity $\hat{v}$ and acoustic pressure $\hat{p}'$ at the driver's diaphragm is given by the formula

$$\left[Z_e Z'_m + (Bl)^2\right] \hat{v} - Bl\hat{u} - Z_e S_d \hat{p}' = 0, \tag{5.8}$$

see Fig. 2, where

Electrical parameters	
R_v	Electrical resistance of the voice coil
L_v	Electrical inductance of the voice coil (at low frequencies)
R_2	Electrical resistance of the voice coil due to eddy currents
L_2	Para-inductance of the voice coil (at high frequencies)
Mechanical parameters	
m_m	Mass of a moving assembly (diaphragm, voice coil)
c_m	Suspension compliance
r_m	Mechanical resistance (mechanical losses)
Acoustical parameters	
c_a	Compliance of the air behind the diaphragm
Z_a	Radiation impedance

Table 1: List of symbols used in Fig. 2.

$$Z_e = R_v + \mathrm{i}\omega L_v, \tag{5.9}$$

$$Z'_m = Z_m + \frac{S_d^2}{\mathrm{i}\omega c_a}, \tag{5.10}$$

where

$$Z_m = r_m + \mathrm{i}\omega m_m + \frac{1}{\mathrm{i}\omega c_m}. \tag{5.11}$$

Inserting Eq. (5.8) into boundary conditions given in Eq. (5.4) results in

$$\left[Z_e Z'_m + (Bl)^2\right] \left.\frac{\mathrm{d}\hat{\varphi}}{\mathrm{d}x}\right|_{x=l} - Bl\hat{u} - Z_e S_d \mathrm{i}\omega\rho_0\hat{\varphi}|_{x=l} = 0, \tag{5.12a}$$

$$\left.\frac{\mathrm{d}\hat{\varphi}}{\mathrm{d}x}\right|_{x=0} = 0. \tag{5.12b}$$

6

ACOUSTICALY GENERATED TURBULENCE

In the following we will be dealing mostly with resonators with variable cross-section. As shown in [37] these so-called dissonant resonators possess an important characteristic - their higher resonant modes are at frequencies that are not integer multiples of the fundamental resonance frequency. In effect non-linear energy transfer from the fundamental resonance to higher harmonic resonances is severely suppressed. As shown in [31] in such a situation harmonic generation accounts for only about 10 % to 20 % of the excess losses that exceed linear losses. Most significant factor contributing to energy losses in shaped resonators which suppress harmonic generation is the increasing effective viscosity and thermal conductivity associated with acoustically generated turbulence [31]. In the following section losses due to turbulence in the boundary layer are estimated using the eddy viscosity model. It is assumed that losses due to turbulence in the volume of the resonator are negligible compared to the losses due to turbulence in the boundary layer.

Viscosity coefficient can be expressed as

$$\eta_t = \eta + \eta_e, \tag{6.1}$$

where η_t is the total viscosity, η is the shear (dynamic) viscosity and η_e is the eddy viscosity which can be expressed as

$$\eta_e = \zeta_r \eta \left(\sqrt{1 + \left(\frac{\mathrm{Re}}{\mathrm{Re}_0} \right)^2} - 1 \right), \tag{6.2}$$

where ζ_r characterizes the ratio between the shear viscosity and the eddy viscosity and is determined by matching measured and calculated dissipation. Re is the Reynolds number in the boundary layer and can be expressed as

$$\mathrm{Re} = \frac{\sqrt{2} M c_0 \delta_t}{\nu}, \tag{6.3}$$

where M is the Mach number in the boundary layer and δ_t is the boundary layer thickness given by [36]

$$\delta_t = \sqrt{\frac{2\nu_t}{\omega}}, \tag{6.4}$$

where ν_t is the total kinematic viscosity $\nu_t = \eta_t / \rho_0$. Re_0 is the Reynolds number at which transition to turbulence occurs $\mathrm{Re} = \mathrm{Re}_0 = 400$. Using the equations above we can express

$$\frac{\eta_t}{\eta} = \tilde{\nu_t} = 1 + \zeta_r \left(\sqrt{1 + \beta M^2 \tilde{\nu_t}} - 1 \right), \tag{6.5}$$

where $\tilde{\nu_t} = \nu_t / \nu = \eta_t / \eta$ is the normalized kinematic viscosity coefficient,

$$\beta = \frac{4 \mathrm{Re}_1 \omega_0}{\pi \mathrm{Re}_0^2 \omega}, \tag{6.6}$$

where $\omega_0 = \pi c_0 / l_r$ and

$$\mathrm{Re}_1 = \frac{\rho_0 c_0 l_r}{\eta_0}, \tag{6.7}$$

where l_r is the length of the resonator. Normalized kinematic viscosity coefficient can be therefore expressed as

$$\tilde{\nu_t} = \kappa + \sqrt{\kappa^2 + 2\zeta_r - 1}, \tag{6.8}$$

where

$$\kappa = 1 - \zeta + \frac{\zeta_r^2 \beta M^2}{2}. \tag{6.9}$$

Eddy viscosity is taken into account by multiplying the kinematic viscosity parameter in Eq. (3.11) with the normalized kinematic viscosity coefficient $\tilde{\nu}$ given in Eq. (6.5). Equation (3.11) is then then modified into

$$\epsilon_t = \sqrt{\nu \tilde{\nu_t}} \left(1 + \frac{\gamma - 1}{\sqrt{Pr}} \right). \tag{6.10}$$

Substituting ϵ with ϵ_t in the system of equations (4.15) for numerical solution of the non-linear model equation Eq. (3.25) results in the following system of equations

$$\frac{\mathrm{d}\Phi_k}{\mathrm{d}X} = \frac{W_k}{R^2}, \tag{6.11a}$$

$$\begin{aligned} \left(1 - \frac{\sqrt{\tilde{\nu}\Gamma}}{\sqrt{\mathrm{i}k\Omega}R} \right) \frac{\mathrm{d}W_k}{\mathrm{d}X} = -k^2\pi^2\Omega^2 R^2 \Phi_k + \mathrm{i}k \frac{\pi^2 \Omega}{R^2} \sum_{j=k-N}^{N} W_{k-j} W_j - \\ - \mathrm{i}k\pi^4 \Omega^3 \frac{\gamma - 1}{2} R^2 \sum_{j=k-N}^{N} (k-j)\, j \Phi_{k-j} \Phi_j + \mathrm{i}k\pi^2 \Omega R^2 X A_k + \\ + \mathrm{i}k^3 \pi G \Omega^3 R^2 \Phi_k - \frac{\sqrt{\tilde{\nu}\Gamma}}{\sqrt{\mathrm{i}k\Omega}R^2} \frac{\mathrm{d}R}{\mathrm{d}X} W_k. \end{aligned} \tag{6.11b}$$

Likewise replacing ϵ with ϵ_t in the system of equations (5.5) for solving linear model equation (5.3) results in

$$\frac{\mathrm{d}\Phi}{\mathrm{d}X} = \frac{W}{R^2}, \tag{6.12a}$$

$$\left(1 - \frac{\sqrt{\tilde{\nu}\Gamma}}{\sqrt{\mathrm{i}\Omega}} \right) \frac{\mathrm{d}W}{\mathrm{d}X} = -\pi^2 \Omega^2 R^2 \left(1 - \frac{\mathrm{i}G\Omega}{\pi} \right) \Phi - \frac{\sqrt{\tilde{\nu}\Gamma}}{\sqrt{\mathrm{i}\Omega}R^2} \frac{\mathrm{d}R}{\mathrm{d}X} W. \tag{6.12b}$$

7

RESONATOR SHAPE OPTIMIZATION

7.1 INTRODUCTION

There is an infinite number of different shapes the resonator can have. Each shape having a different frequency response characteristic where different maximum acoustic pressures correspond to different frequencies. The optimisation problem is defined as follows: find a shape of an acoustic resonator, subject to a given set of constraints (e. g. geometrical), which maximizes the attained acoustic pressure amplitude inside the resonator. To ensure that the searched shape-space is sufficiently general (i. e. not limited to a simple elementary functions) individual shapes will have to be defined by a number of parameters. These parameters could for example serve as coordinates of a control points using which the resonator shape is reconstructed by the means of interpolation (using polynomials or a spline). This means that the space of possible resonator shapes (search space) will be very complex (multi-dimensional) possibly with many local optima. As can be seen in Fig. 3 even a two-dimensional optimisation problem can have a very complex search space and finding the global optimum can be a rather difficult task. Simple methods (e. g. gradient-based optimization) are of no use because they tend to get stuck in local optima. Different methods for solving this kind of problems have been proposed in the past such as random searches, simulated annealing, and others (see e. g. [13]). Some of the most successful methods have

proved to be random searches motivated by analogies with the natural selection – evolutionary algorithms.

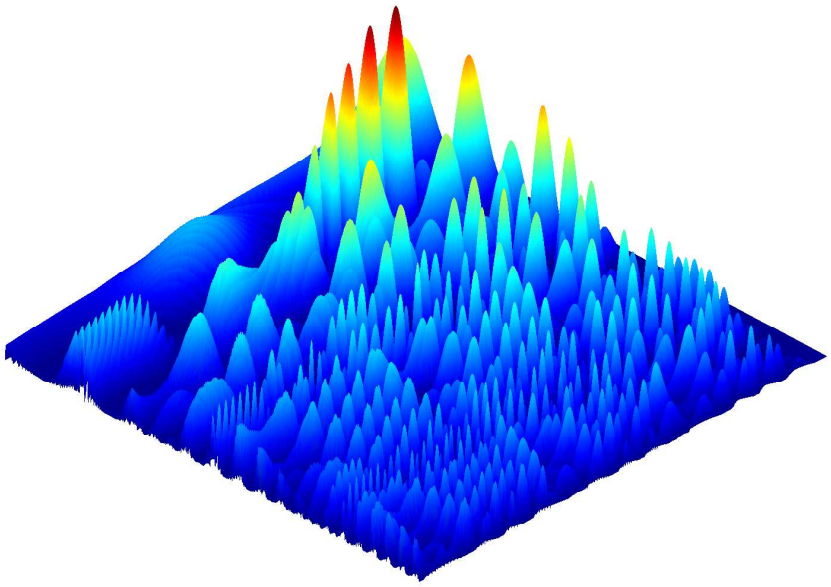

Figure 3: Example of a complex search space of a two-dimensional optimisation problem.

7.2 EVOLUTIONARY ALGORITHMS

Evolutionary algorithms are population-based optimization algorithms inspired by the processes of natural evolution and are a subset of a broader field called Evolutionary computation. The three main branches of Evolutionary algorithms are Genetic algorithms, developed by Holland [25], Evolutionary strategies, developed by Rechenberg and Schwefel [48] and Evolutionary programming, developed by Fogel [19]. These

algorithms, in many ways similar to each other, all borrow ideas from the field of evolutionary biology, i. e. take advantage of the collective learning process of the population of individuals and use mechanisms that mimic the processes of natural evolution.

Generally, the optimisation process has the following structure. The algorithm starts with a *population* of *individuals* (candidate solutions to the optimisation problem) which are spread randomly throughout the search space. The population is then navigated towards the global optimum over series of steps (*generations*) by means of a randomized process of *selection*, *mutation* and (depending on the method) *recombination*. The quality of different candidate solutions – their *fit* is measured by means of objective function to be optimized. Individuals with higher fitness value have a better chance to be promoted by the selection operator to become parents of the next generation than those with lower fitness value. Recombination operator (analogous to the sexual reproduction) determines how offspring are created from the parent population. Mutation operator introduces (small) change to the offspring population thereby preventing the loss of diversity in the population.

Evolutionary algorithms are general and since they usually do not make any assumptions about the underlying fitness landscape, they can be successfully applied to a wide range of different problems. Application of these algorithms to the real-world problem has shown that evolutionary algorithms are capable of solving large-scale complex problems with their complex search spaces riddled with multiple local optima (e. g. [3]).

Notation introduced in Tab. 2 will be used throughout.

In the following section short overview of the three algorithms is presented.

$f : \mathbb{R}^n \to \mathbb{R}$	Objective function to be optimized
I	Space of individuals
$\boldsymbol{z}$	Vector of object variables
$\boldsymbol{a} \in I$	Individual
μ	Number of parents
λ	Number of offspring
$\Phi : I \to \mathbb{R}$	Fitness function
$P(t) = \{\boldsymbol{a}_1(t), ..., \boldsymbol{a}_\mu(t)\}$	Population at generation t
$r : I^\mu \to I^\lambda$	Recombination operator
$m : I^\lambda \to I^\lambda$	Mutation operator
$s : \left(I^\lambda \cup I^{\mu+\lambda}\right) \to I^\mu$	Selection operator

Table 2: Notational convention.

7.2.1 *Genetic algorithms (GAs)*

Genetic algorithms are probably the most widely used Evolutionary algorithms. In their original (sometimes called canonical) form proposed by Holland, GAs work with individuals represented by fixed-length strings of binary numbers. This is obviously advantageous for optimization of pseudo-boolean functions but for optimization of continuous-parameter functions, object variables need to be represented by binary numbers. Each individual is divided into a number of segments, where each segment encodes one object variable. This creates a trade-off between size of the individual (number of bits in every string) and accuracy.

In canonical GAs, crossover (recombination operator) plays a dominant role in introducing variation in the population by combining use-

ful segments from different individuals. Standard crossover operator is the one-point crossover which can be expressed in the following way: if $\boldsymbol{s} = (s_1, ..., s_l)$ and $\boldsymbol{v} = (v_1, ..., v_l)$ are two parents selected for reproduction by selection operator, one-point crossover creates two offspring $\boldsymbol{s'}$ and $\boldsymbol{v'}$ according to the formula

$$\begin{aligned} \boldsymbol{s'} &= (s_1, ..., s_{\chi-1}, s_\chi, v_{\chi+1}, ..., v_l), \\ \boldsymbol{v'} &= (v_1, ..., v_{\chi-1}, v_\chi, s_{\chi+1}, ..., s_l), \end{aligned}$$

where $\chi \in \langle 1..l \rangle$ is a uniform random variable.

Crossover in GAs works directly on the bit string - ignoring the semantic boundaries between the encoded variables. Exogenous parameter p_c is usually employed which determines whether parents undergo crossover or they are passed to next generation unchanged. The usual values of p_c are in the range $\langle 0.5, 1.0 \rangle$.

Mutation operator in GAs has only a secondary role. Same as crossover operator - it works directly on the bit strings - occasionally inverting single bits with the probability p_m (p_m is usually a very small number $p_m \approx 10^{-3}$). Since mutation operator inverts bits randomly - resulting change in phenotype is arbitrarily large.

Selection operator in GAs is a probabilistic, fitness-dependent one. Usually a so-called roulette-wheel selection is implemented where the probability of an individual $\boldsymbol{a_i}$ being selected to become a parent is given by its relative fitness

$$P(\boldsymbol{a}_i) = \frac{\Phi(\boldsymbol{a}_i)}{\sum_{j=1}^{\mu} \Phi(\boldsymbol{a}_j)}. \tag{7.1}$$

The method is analogous to the turning of a roulette wheel which is divided into μ segments representing the individuals. The size of each

segment is proportional to the fitness of an individual it represents. This selection operator is *preservative*, i. e. even individual with worst fitness has non-zero chance to pass its *genes* to the next generation.

7.2.2 *Evolutionary programming (EP)*

Evolutionary programming differs from GAs in several important aspects. Most importantly it works directly with real-valued object variables, i. e. it works directly on the phenotype and is not concerned with a genetic-level abstraction. Furthermore Evolutionary programming relies entirely on mutation as a means of introducing variation – recombination operator is not used at all. Individual $\boldsymbol{a}$ is represented by the vector of object variables $\boldsymbol{z}$ and a vector of strategy parameters $\boldsymbol{\nu}$ which determine the rate of mutation for every object variable, $\boldsymbol{a} = (\boldsymbol{z}, \boldsymbol{\eta})$.

In general mutation can be expressed as

$$\boldsymbol{z'} = \boldsymbol{z} + \Delta\boldsymbol{z}, \tag{7.2}$$

where $\boldsymbol{z}$ is a vector of object variables before mutation, $\boldsymbol{z'}$ is a vector of object variables after mutation and $\Delta\boldsymbol{z}$ is the mutational step size vector. Mutation step size is determined by strategy parameters and a random variable sampled from some probability distribution. Gaussian distribution is the most common one however other distributions can also be used e. g. Cauchy, Lévy, etc. (see e. g. [2]). Using Gaussian distribution together with self-adapting strategy parameters (strategy parameters evolve together with object variables) offspring is generated using

$$
\begin{aligned}
z'_{i,j} &= z_{i,j} + \eta_{i,j}\mathcal{N}_{i,j}\left(0,1\right), \\
\eta'_{i,j} &= \eta_{i,j} e^{\tau' \mathcal{N}_i(0,1) + \tau \mathcal{N}_{i,j}(0,1)},
\end{aligned} \tag{7.3}
$$

where subscripts i and j denote i-th individual and j-th component of the vectors $\boldsymbol{z}$, $\boldsymbol{z'}$, $\boldsymbol{\eta}$ and $\boldsymbol{\eta'}$. $\mathcal{N}\left(0,1\right)$ is a normally distributed one-dimensional random variable with mean zero and standard deviation $\sigma = 1$. $\mathcal{N}_i$ is generated anew for every individual, $\mathcal{N}_{i,j}$ is generated anew for every j and

$$
\begin{aligned}
\tau &= \frac{1}{\sqrt{2\sqrt{n}}}, \\
\tau' &= \frac{1}{\sqrt{2n}},
\end{aligned} \tag{7.4}
$$

where n is the number of object variables (size of the vector $\boldsymbol{z}$).

Same as GAs, Evolutionary programming uses probabilistic, fitness-dependent selection operator in the form of tournament selection. For each parent $\boldsymbol{a} = (\boldsymbol{z}, \boldsymbol{\eta})$ and each offspring $\boldsymbol{a'} = (\boldsymbol{z'}, \boldsymbol{\eta'})$, q[1] opponents are randomly chosen from the pool of all parents and all offspring. For each comparison, if the individual's fitness is better than the opponent's it receives a "win". μ individuals that have most "wins" are then selected from all parents and all offspring creating new generation. This selection operator is *extinctive*, i. e. individuals with low fitness die out and *elitist*, i. e. individual with highest fitness is guaranteed tu survive.

1 q being exogenous parameter.

7.2.3 *Evolutionary strategies (ES)*

Evolutionary strategies, though developed independently, are rather similar to Evolutionary programming. Both are known as Phenotypic algorithms – they both operate directly on object variables whereas GAs (Genotypic algorithm) operate on bit strings that represent object variables. Same as in Evolutionary programming the individual has two components, vector of object variables $\boldsymbol{z}$ and vector of standard deviations (strategy parameters) $\boldsymbol{\sigma}$ such that $\boldsymbol{a} \in I = \mathbb{R}^{2n}$. Sometimes it is useful to work with only one common standard deviation, i. e. $\boldsymbol{a} \in I = \mathbb{R}^{n+1}$.

Similarly to Evolutionary programming, mutation can be expressed as

$$\sigma'_{i,j} = \sigma_{i,j} e^{\tau' \mathcal{N}_i(0,1) + \tau \mathcal{N}_{i,j}(0,1)}, \tag{7.5}$$

$$z'_{i,j} = z_{i,j} + \sigma_{i,j} \mathcal{N}_{i,j}\left(0,1\right). \tag{7.6}$$

Most important difference between Evolutionary programming and Evolutionary strategies is that the latter uses recombination operator. Several different recombination mechanisms have been proposed. Offspring can either be created from two randomly selected parents or in its global form the recombination mechanism creates offspring with components from potentially all individuals in parent population. Furthermore recombination is applied also to standard deviations vector and recombination operator for object variables and standard deviations need not to be the same. Description of different recombination mechanisms is summarized in Table 3.

Subscripts S and T denote two different individuals selected randomly from parent population and $\chi \in \langle 0, 1 \rangle$ is a uniform random variable. In

Offspring z'_i component	Description
$z_{S,i}$	No recombination
$z_{S,i}$ or $z_{T,i}$	Discrete recombination
$z_{S,i} + \chi\left(z_{T,i} - z_{S,i}\right)$	Intermediate recombination
$z_{S_i,i}$ or $z_{T_i,i}$	Global discrete recombination
$z_{S_i,i} + \chi_i\left(z_{T_i,i} - z_{S_i,i}\right)$	Global intermediate recombination

Table 3: Different types of recombination mechanisms in Evolutionary strategies.

global variants, for each component z_i, both parents S_i and T_i as well as χ_i are sampled anew.

Selection operator, unlike in the other two algorithms is completely deterministic selecting μ ($1 \leq \mu \leq \lambda$) best individuals from the set of λ offspring (termed (μ,λ)-ES) or from the union of all offspring and parents (termed (μ+λ)-ES). In most cases (μ,λ)-ES is a preferred strategy with an optimal ratio for $\mu/\lambda \approx 1/7$. This selection operator is extinctive.

7.2.4 *Summary*

Main characteristics of the three evolutionary algorithms are summarized in the following table.

Brief discussion above describes the three evolutionary algorithms in their standard form. There are different variants of these algorithms using operators implemented in different manner (this is especially true for GAs). More in-depth discussion can be found in [2].

	GAs	EP	ES
Representation	Binary-valued	Real-valued	Real-valued
Self-adaptation	No	Yes	Yes
Mutation	Background operator	Only operator	Main operator
Recombination	Main operator	None	Yes
Selection	Probabilistic, preservative	Probabilistic, extinctive, elitist	Deterministic, extinctive

Table 4: Main characteristics of Evolutionary algorithms.

7.3 OPTIMIZATION PROCEDURE

7.3.1 *Description of the resonator shape*

As mentioned before, in order not to limit ourselves to a set of pre-defined shapes given by elementary functions (exponential, conical, trigonometric), resonator shape is defined using N control points (object variables) distributed regularly along the resonators axis of symmetry[2] at positions

$$x_i = \frac{il}{N-1}, \qquad i = 0, 1, ..., N-1, \tag{7.7}$$

where l is the length of the resonator. Generally resonator shape can be expressed as

2 We assume axi-symmetrical resonator.

$$r\left(x\right) = r\left(x, \{[x_i, r_i]\}\right), \tag{7.8}$$

where $r\left(x\right)$ is resonator radius at x and $[x_i, r_i]$ are control point pairs. The resonator shape $r\left(x\right)$ between the control points is obtained using the cubic-spline interpolation.

7.3.2 *Handling of constraints*

Due to the nature of the problem we define constraints for two types of parameters. Geometrical constraints – resonator radius $r(x)$ is required to stay within some pre-specified bounds

$$r_{min} \leq r(x) \leq r_{max}, \qquad x \in \langle 0, l \rangle . \tag{7.9}$$

Also it might be desirable to restrict the resonance frequency of the loudspeaker-resonator system to a certain limits

$$f_{min} \leq f_r \leq f_{max}. \tag{7.10}$$

If the individual meets both conditions we say that the individual lies in the feasible parameter area. If it does not comply with any (or both) of the conditions, it lies in the infeasible parameter area. Feasible area is a rectangle defined by lower and upper boundary values for each parameter. Situation is shown in Fig. 4. In our algorithm parameter constraints are accounted for by introducing a penalty term in the fitness function. This penalty term measures the distance of the constrained parameter from the feasible area.

For geometrical parameters we use a box boundary handling algorithm [24] such that each evaluated individual is guaranteed to lie in

the feasible area. If resonator radius at x_{if} lies outside the feasible area ($r(x_{if}) < r_{min} \vee r(x_{if}) > r_{max}$) the objective function of the corresponding individual is evaluated at

$$r'\left(x_{if}\right) = r_{\text{feas}}\left(x_{if}\right), \tag{7.11}$$

where $r_{\text{feas}}(x_{if})$ is the closest feasible radius (with minimal $|r_{\text{feas}}(x_{if}) - r(x_{if})|$), i. e. resonator radius is clipped on the boundary of feasible area. The new feasible individual (resonator shape) is used for objective function evaluation only and is discarded afterwards. Penalty term p_g that measures the distance from the feasible area is calculated using the following equation

$$p_g = \max\left(\frac{|r_{\text{feas}}\left(x\right) - r\left(x\right)|}{r_{max} - r_{min}}\right), \qquad \forall x \in \langle 0, l\rangle\,. \tag{7.12}$$

Resonance frequency constraints are accounted for by introducing the penalty term p_f in the following way

$$p_f = \frac{|f_{r_{\text{feas}}} - f_r|}{\frac{f_{max} + f_{min}}{2}}, \tag{7.13}$$

where $f_{r_{\text{feas}}}$ is the closest boundary of the feasible area.

If the individual mutates into the infeasible area it is evaluated there and the corresponding penalty term is added to the fitness function described below.

7.3.3 *Fitness function evaluation*

The optimisation criterion is the one for maximisation of the objective function – the acoustic pressure amplitude at the resonance frequency at

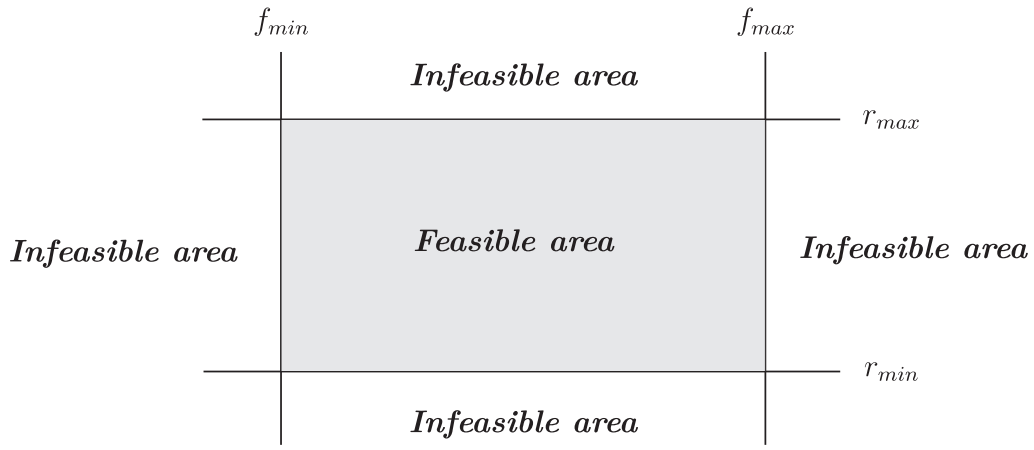

Figure 4: Boundaries.

one of the resonator ends ($x = 0$). Mathematically, it can be expressed as

$$f(\boldsymbol{z}) = \frac{|\hat{p}'(x = 0, \Omega = \Omega_{resonance})|}{|\hat{u}|}. \tag{7.14}$$

Fitness function of an individual $\boldsymbol{a} = (\boldsymbol{z}, \boldsymbol{\sigma})$ is calculated by adding the penalty terms

$$\Phi(\boldsymbol{a}) = f(\boldsymbol{z})(1 - p_g)(1 - p_f)^2. \tag{7.15}$$

It is important to note that the fitness function of the resonator depends on the length of the resonator (due to frequency-dependence of the losses), maximum and minimum radii r_{max}, r_{min} and on the physical parameters of the loudspeaker model.

7.3.4 *Algorithm*

Because of the nature of the problem at hand (optimization of continuous parameters) Evolutionary strategies of the (μ, λ)-ES type were chosen as optimization algorithm.

The algorithm starts by generating a population of μ random individuals according to the following formula.

$$\boldsymbol{a_i} = (\boldsymbol{z_i}, \boldsymbol{\sigma_i}), \qquad i = 1...\mu, \tag{7.16}$$

where

$$z_{i,j} = r_{min} + (r_{max} - r_{min})\,\chi_{i,j},$$
$$\sigma_{i,j} = \sigma_0,$$

where $\chi \in \langle 0, 1\rangle$ is a uniform random variable and σ_0 is the initial standard deviation. After the initial population is created, algorithm proceeds to the evolution. First, μ parents are recombined to produce λ offspring. Offspring population is then mutated using equations (7.5) and (7.6). The fitness function of each individual in the mutated offspring population is then evaluated using Eq. (7.15)[3] and the best μ individuals are selected as parents for a next generation. This process of recombination, mutation and selection is then repeated until pre-defined termination criterion is met. The termination criterion used in our algorithm is the following: if

3 Acoustic field inside the resonator is computed numerically using equation (5.5). Boundary value problem is solved using the shooting method. Resonance frequency f_r and acoustic pressure at resonance $p_{f=f_r}$ are found using the golden section search [45].

the all-time best fitness is not improved in the last t_{term} generations the optimization algorithm is terminated.

A pseudo-code description of the optimization algorithm is shown in Algorithm 1.

Algorithm 1 Optimization of the resonator shape

1: $\mu \leftarrow$ Number of parents
2: $\lambda \leftarrow$ Number of offspring
3: $n \leftarrow$ Number of object variables
4: $\sigma_0 \leftarrow$ Initial standard deviation
5: $t_{term} \leftarrow$ Termination criterion
6: $r_{min} \leftarrow$ Minimal radius
7: $r_{max} \leftarrow$ Maximal radius
8: $f_{min} \leftarrow$ Minimal resonance frequency
9: $f_{max} \leftarrow$ Maximal resonance frequency
10: $l \leftarrow$ Resonator length
11: $speak \leftarrow$ Loudspeaker parameters
12: Global $BI \leftarrow$ [] /*Best individual*/
13: Global $BF \leftarrow 0.0$ /*Best fitness*/

1: $OptimalShape = Optimization(\mu, \lambda, n, \sigma_0, t_{term}, r_{min}, r_{max}, f_{min}, f_{max}, l, speak)$

2: **function** $Optimization(\mu, \lambda, n, \sigma_0, t_{term}, r_{min}, r_{max}, f_{min}, f_{max}, l, speak)$

3: $Parents \leftarrow GenerateRandomPopulation(\mu, \sigma_0, n, l, r_{min}, r_{max})$
4: **while** Termination criterion not met **do**
5: $\quad Offspring = Recombination(Parents, \lambda)$
6: $\quad Offspring' = Mutation(Offspring)$
7: $\quad Parents = Selection(Offspring', BI, BF, \mu, \lambda, r_{min}, r_{max}, f_{min}, f_{max}, speak)$
8: **end while**
9: **return** BI

1: **function** $Selection(Population, BI, BF, \mu, \lambda, r_{min}, r_{max}, f_{min}, f_{max}, speak)$

2: **for** $i = 0$ to $\lambda - 1$ **do**

3: $f_s \leftarrow GetFundamentalResonanceFreq(Population(i), speak)$

4: $p' \leftarrow GetAcousticPressureAmplitude(Population(i), speak, f_s)$

5: $Fitness(i) = GetFitness(Population(i), p', f_s, r_{min}, r_{max}, f_{min}, f_{max})$

6: **end for**

7: $Sort(Population, Fitness)$

8: **if** $Fitness(0) > BF$ **then**

9: $BI = Population(0)$

10: $BF = Fitness(0)$

11: **end if**

12: **return** $Population(0, 1, ..., \mu - 1)$

Part II

EXPERIMENTAL PART

8

EXPERIMENTAL VERIFICATION OF THE LOUDSPEAKER-RESONATOR MODEL

In the following section the theoretical model of the loudspeaker-acoustic resonator system developed in previous chapters is compared with an experiment. Results are presented for two different resonators - cylindrical and conical. The experimental setup is shown in Fig. 5.

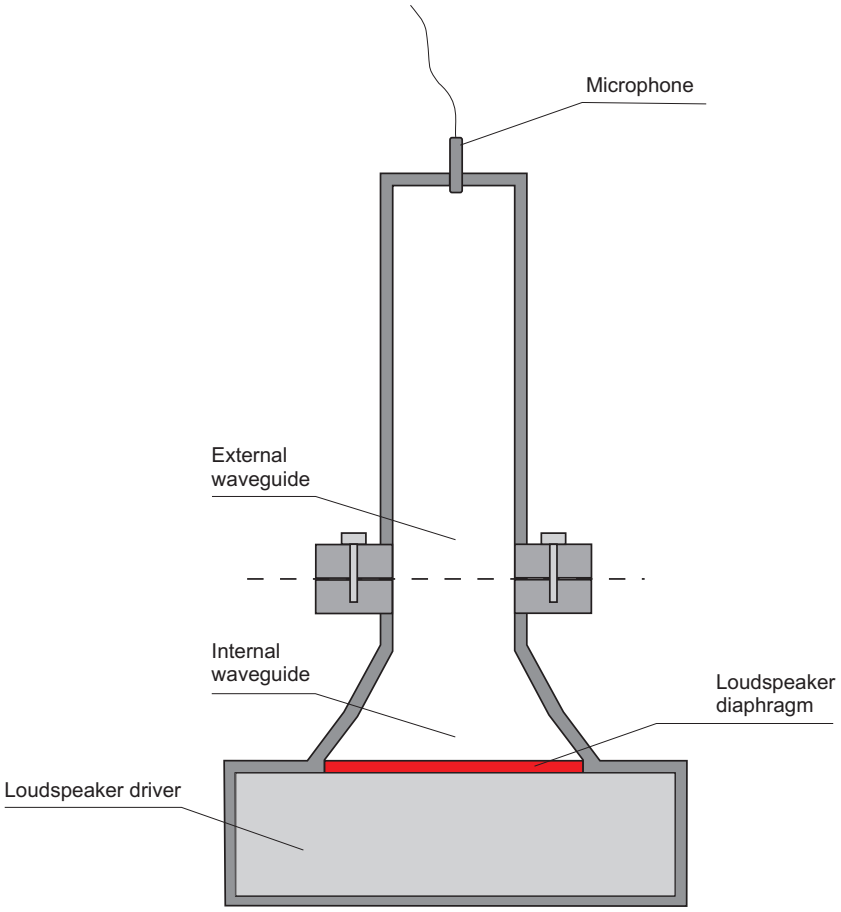

Figure 5: Experimental setup.

8.1 LOUDSPEAKER

Compression driver Selenium DT-405Ti was chosen for experiments. Linear parameters of the Selenium driver were determined by fitting the measured electrical input impedance characteristic and measured diaphragm displacement characteristic with their modelled counterparts (details given in the appendix A).

For better impedance matching, compression drivers usually utilize a so-called phase plug, placed between the diaphragm and the (external) waveguide throat, acting as an impedance transformer. Since this is not desirable in our application the phase plug was removed from the driver creating a short waveguide (internal waveguide). This short waveguide inside the driver has a rather complex shape and for the purpose of modelling had to be approximated (approximated geometry is shown in Fig. 6). Formula describing the shape of the approximated internal waveguide as well as the measured linear parameters of the Selenium loudspeaker are shown in the appendix A.

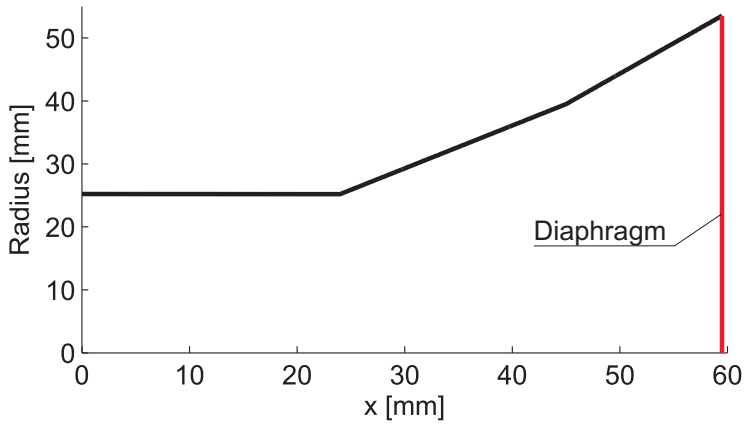

Figure 6: Approximated internal waveguide inside the Selenium DT-405Ti compression driver with the phase plug removed from the driver.

8.2 LOUDSPEAKER-RESONATOR SYSTEM

Resonator cavity is formed by the internal waveguide inside the driver and external waveguide attached to the driver. The total resonator length l is therefore given by

$$l = l_{int} + l_{ext}, \tag{8.1}$$

where l_{int} is the length of the internal waveguide and l_{ext} is the length of the external waveguide.

Experiments were performed with two different (external) resonators, cylindrical and conical (shown in Fig. 7). Both resonators were $l_{ext} = 300\,\text{mm}$ long with throat radius $r_t = 25\,\text{mm}$.

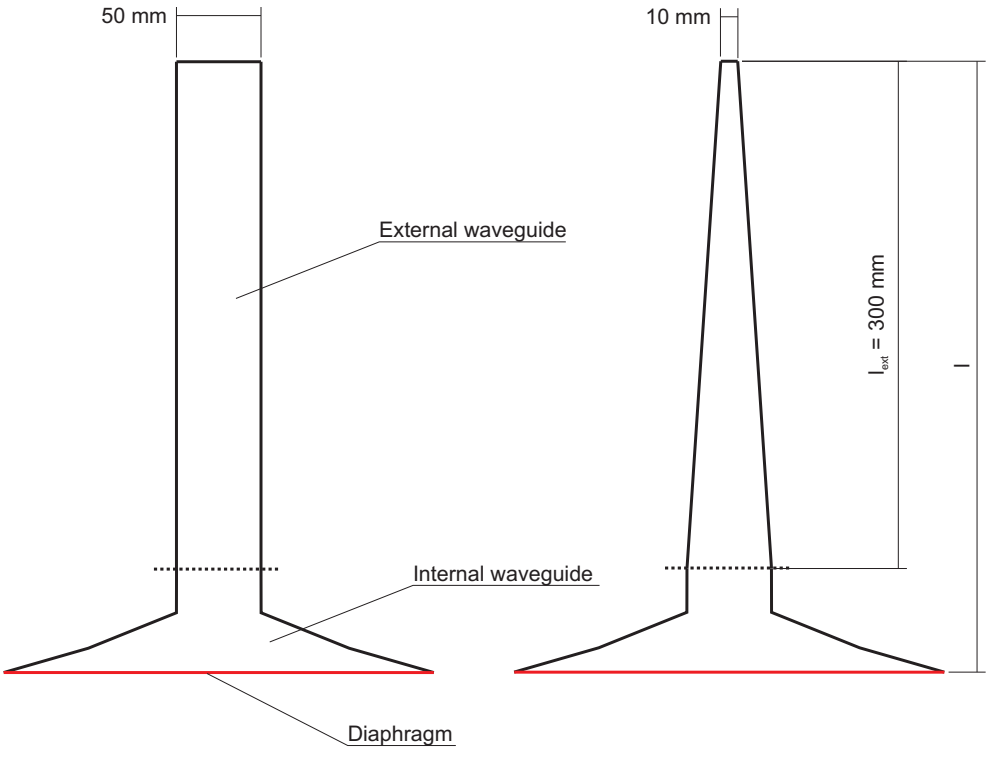

Figure 7: Shapes of the resonator cavities used for the experiment.

8.3 RESULTS

Fig. 8 shows measured and computed frequency characteristics for the cylindrical resonator and Fig. 9 shows measured and computed frequency characteristics for the conical resonator for four different input voltage amplitudes ($|U_1| = 1\,V$, $|U_2| = 5\,V$, $|U_3| = 10\,V$, $|U_4| = 15\,V$).

Acoustic pressure was measured using the NI PCI-6251 measurement card and the G.R.A.S. 12AA pre-amplifier with the G.R.A.S. 40DP microphone which was placed at the closed end of the resonator, $x = 0\,\mathrm{mm}$ (the loudspeaker diaphragm is assumed to be at $x = l$).

Frequency response characteristic was computed from Eq. (6.12) with the turbulence coefficient $\zeta_r = 0.48$. Equations were integrated numerically using the adaptive-stepsize eight-order Runge-Kutta method [45]. Boundary value problem was solved using the shooting method (details can be found in [45]). All numerical calculations were performed assuming the resonator cavity was filled with air at room conditions ($c_0 = 345.2\,\mathrm{m/s}$, $\rho_0 = 1.21\,\mathrm{kg/m^3}$, $\gamma = 1.402$, $c_p = 1004\,\mathrm{J/kgK}$, $\eta = 1.827 \times 10^{-5}\,\mathrm{kg/ms}$, $\zeta = 1.096 \times 10^{-5}\,\mathrm{kg/ms}$, $\kappa = 25.87\,\mathrm{J/Kms}$).

It can be observed that in both cases an acceptable agreement between theory and measurement is achieved regarding a resonance frequency as well as acoustic pressure amplitudes.

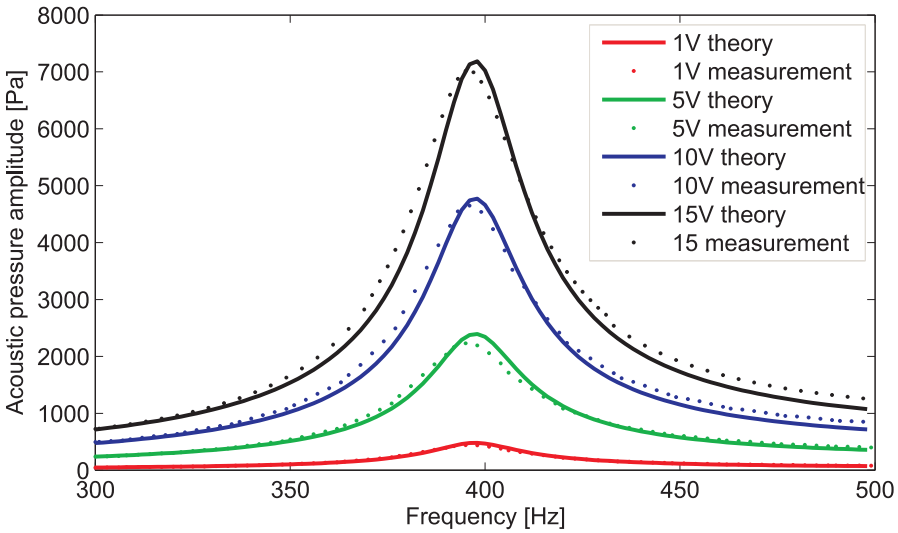

Figure 8: Measured and computed frequency response characteristics of the loudspeaker-resonator system with the cylindrical external resonator.

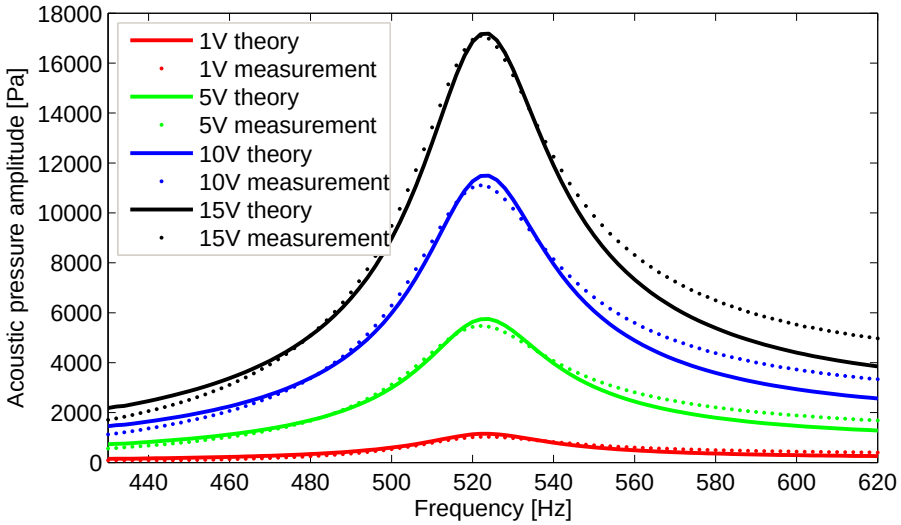

Figure 9: Measured and computed frequency response characteristics of the loudspeaker-resonator system with the conical external resonator.

9

OPTIMISATION RESULTS

In the following chapter results of the optimisation procedure presented in Chapter 7 are shown. Parameter values used in the optimization algorithm are summarized in Table 5.

Parameter	Value
Number of parents	$\mu = 15$
Number of offspring	$\lambda = 10\mu$
Number of control points	$N = 10$
External resonator length	$l_{ext} = 0.3\,\mathrm{m}$
Maximum radius	$r_{max} = 25\,\mathrm{mm}$
Minimum radius	$r_{min} = 5\,\mathrm{mm}$
Termination condition	$t_{term} = 15$
Initial standard deviation	$\sigma_0 = 0.01(r_{max} - r_{min})$

Table 5: Optimization algorithm parameter values.

Length of the optimized (external) resonator was chosen to be fixed $l_{ext} = 0.3\,\mathrm{m}$ so that the resulting shape can be directly compared to the two non-optimized resonators described in the previous chapter. However, because of the nature of the optimisation algorithm, the length of the resonator can also be easily optimized along with its shape. A resonance frequency constraints were not applied (frequency bounds were set to $f_{min} = 1\,\mathrm{Hz}$ and $f_{max} = 10^5\,\mathrm{Hz}$).

The optimisation procedure has been run number of times, each time converging to the same result (finding the same resonator shape). Typical results of a single run are presented in the following section.

9.1 OPTIMISATION RUN

It took 105 generations (15750 objective function evaluations) for the optimization algorithm to meet the termination criterion. Evolution of the fitness function is shown in Fig. 10. A fitness function value of each individual within the offspring population lies in the green-coloured area[1]. A mean fitness function value of all individuals in the offspring population at a given generation is represented by the red-color line. It can be observed that the optimization algorithm is able to find the optimal resonator shape very quickly (converges quickly)[2].

In Fig. 11 the evolution of the mean standard deviation is shown. The mean standard deviation for $i-$th individual in the offspring population is computed using the following formula

$$\bar{\sigma_i} = \frac{\sum_{j=1}^{N} \sigma_{i,j}}{N}. \tag{9.1}$$

Again, a mean standard deviation of each individual within the offspring population lies in the green-coloured area. The red-coloured line represents an average standard deviation in the offspring population at a given generation. For the first roughly 12 generations the mean standard

1 Lower and upper bounds of the green-coloured area represent lowest and highest fitness function value within the offspring generation.

2 It is however possible, if is so desired, to make it even faster, especially the long fine-tuning part of the procedure (long flat part of the characteristic) by defining the smallest allowed mutation step - it makes little sense to optimize the shape with precision significantly better than the manufacturing tolerance allows.

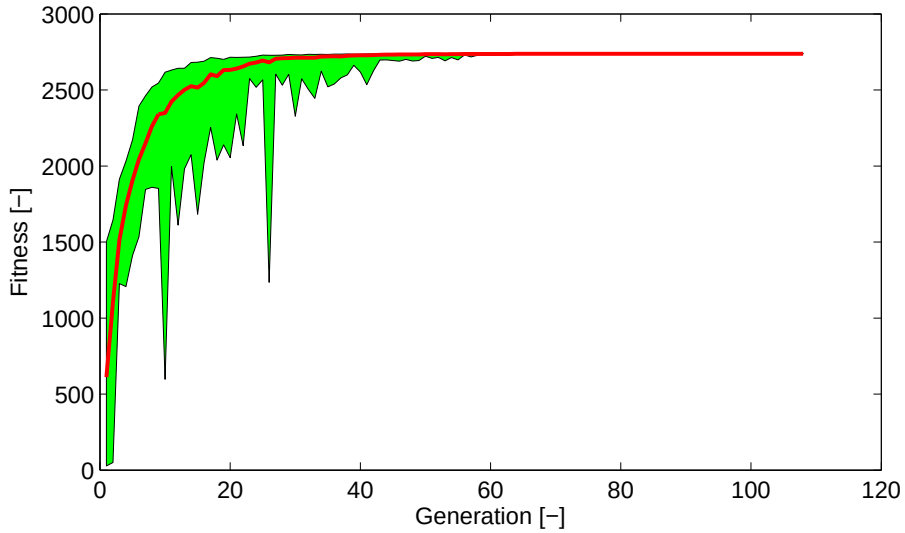

Figure 10: Fitness function evolution. Fitness function value of each individual within the offspring population lies in the green-coloured area. Red-coloured line represents average fitness function value of all individuals within the offspring population.

deviation grows - large mutations are desirable. As the parent population moves closer to the global optimum (and some parameter values get closer to the boundary of the feasible area) smaller mutation is preferred and the mean standard deviation decreases.

The resulting optimum resonator shape[3] (the resonator shape with the all-time best fitness) is shown in Figure 12. Coordinates of the control points (shown as red crosses in Figure 12) are listed in Table 6. As expected the resonator cross-section area gets progressively smaller towards the closed end of the resonator attaining $r = r_{min}$ at $x = 0\,\mathrm{m}$.

The computed frequency response characteristic of the acoustic pressure amplitude at the closed end of the optimized resonator (at $x = 0\,\mathrm{m}$)

3 Optimal resonator shape found by the optimization procedure is valid only for a given loudspeaker, given set of constraints (r_{min}, r_{max}, f_{min}, f_{max}) and resonator length $l = 0.3\,\mathrm{m}$.

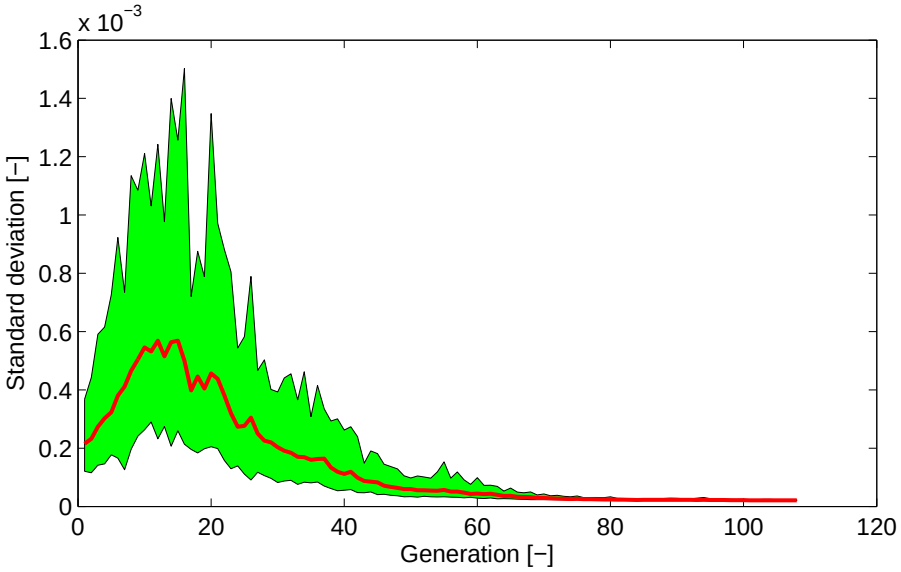

Figure 11: Evolution of the mean standard deviation. Mean standard deviation of each individual within the offspring population lies in the green-coloured area. Red-coloured line represents average standard deviation in the offspring population at a given generation.

x [mm]	0	33.3	66.7	100	133.3	166.7	200	233.3	266.7	300
r [mm]	5	5	5	5.4	7.6	10.6	15.1	23.1	25	25

Table 6: Coordinates of the ten control points for cubic-spline interpolation describing the shape of the optimized resonator.

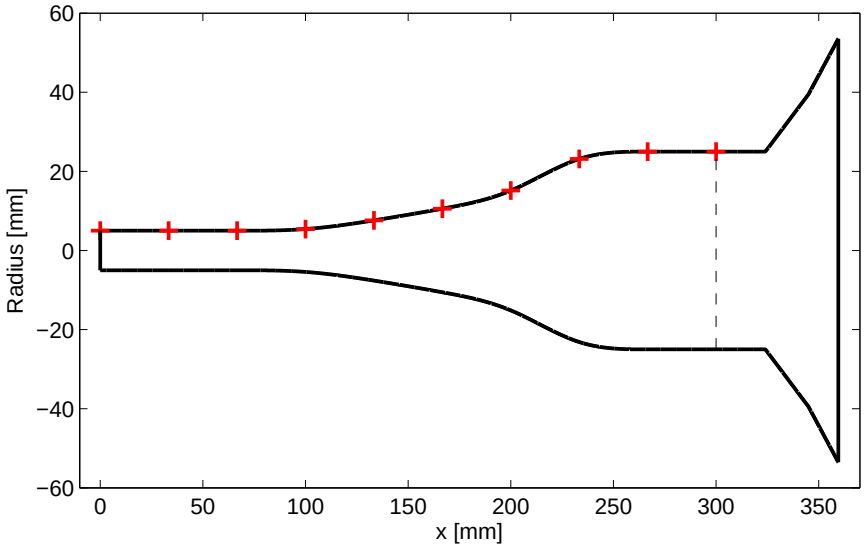

Figure 12: Shape of the resonator with the all-time highest fitness function. Red crosses denote positions of the control points for cubic-spline interpolation. Part of the resonator to the right of the dashed line represents the internal waveguide inside the Selenium driver.

is shown in Fig. 13. The resonance frequency of the loudspeaker-resonator system is 574 Hz. It can be observed that the acoustic pressure amplitude inside the optimized cavity is almost six times greater than in the cylindrical cavity and 2.4 times greater than in the conical cavity. Also worth noting is that the second resonance mode frequency is not twice the fundamental resonance one and therefore we can expect that generation of the second (and higher) harmonics will be severely suppressed because its frequency does not coincide with the resonance mode.

Fig. 14 shows an acoustic pressure amplitude distribution along the spatial coordinate of the optimized resonator driven at the resonance frequency with $|U_{in}| = 1\,\mathrm{V}$ input voltage amplitude.

Fig. 15 shows a velocity amplitude distribution along the spatial coordinate of the optimized resonator driven at the resonance frequency with $|U_{in}| = 1\,\mathrm{V}$ input voltage amplitude.

Fig. 16 and 17 show computed acoustic pressure amplitude and velocity distributions along the spatial coordinate of the optimized resonator versus frequency.

Furthermore, to show the effectiveness of the constraints-handling method, Tab. 7 summarises results of the optimization procedure obtained with different settings of the parameter constraints.

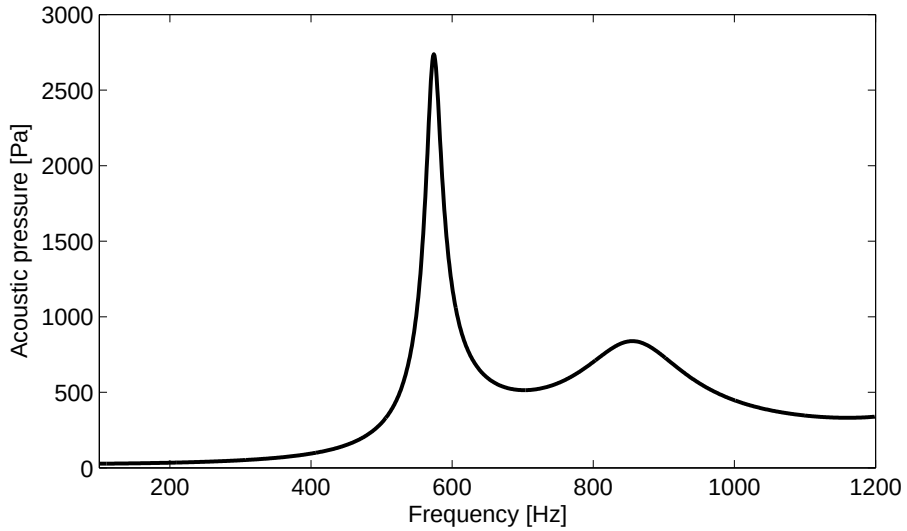

Figure 13: Computed frequency response characteristics of the acoustic pressure amplitude at the closed end of the optimized resonator ($x = 0\,\mathrm{m}$) with $|U_{in}| = 1\,\mathrm{V}$ input voltage amplitude.

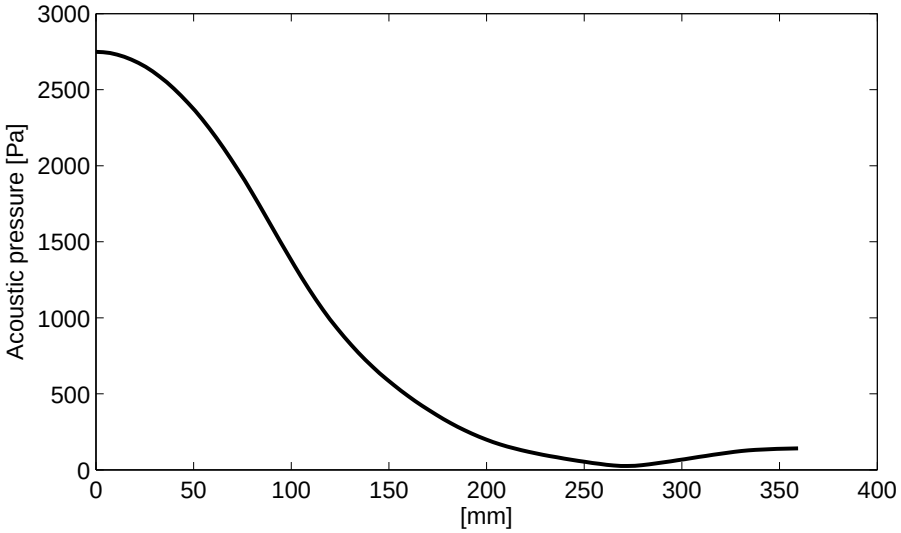

Figure 14: Acoustic pressure amplitude distribution along the spatial coordinate. Resonator driven at the resonance frequency with $|U_{in}| = 1\,\mathrm{V}$ input voltage amplitude.

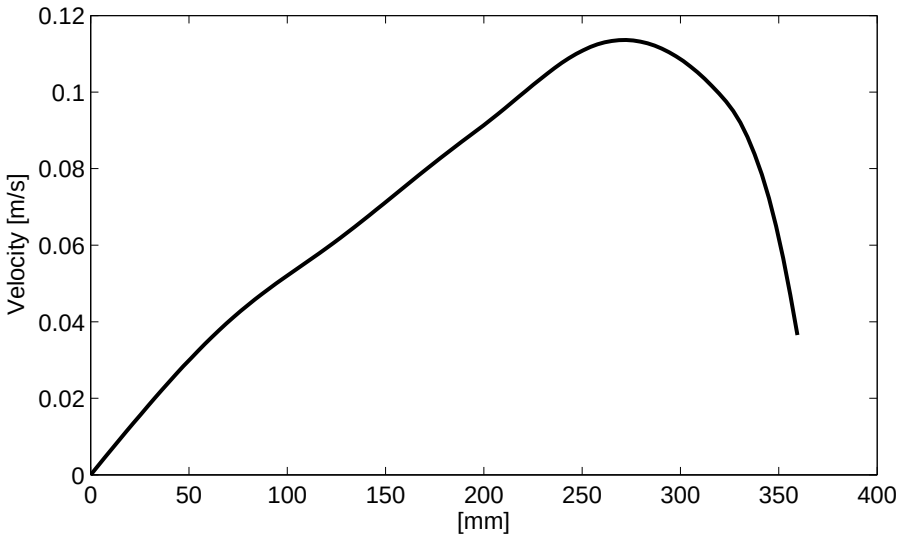

Figure 15: Velocity amplitude distribution along the spatial coordinate. Resonator driven at the resonance frequency with $|U_{in}| = 1\,\mathrm{V}$ input voltage amplitude.

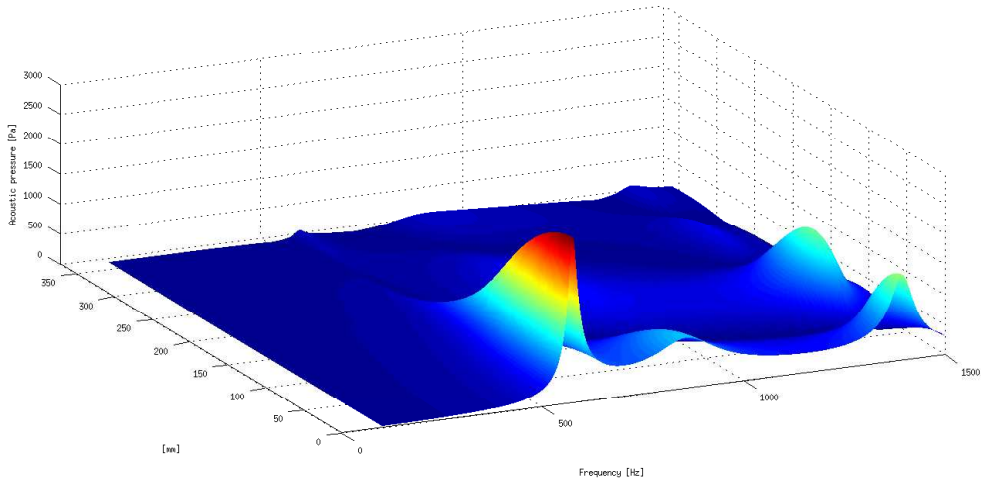

Figure 16: Acoustic pressure amplitude distribution along the spatial coordinate versus frequency.

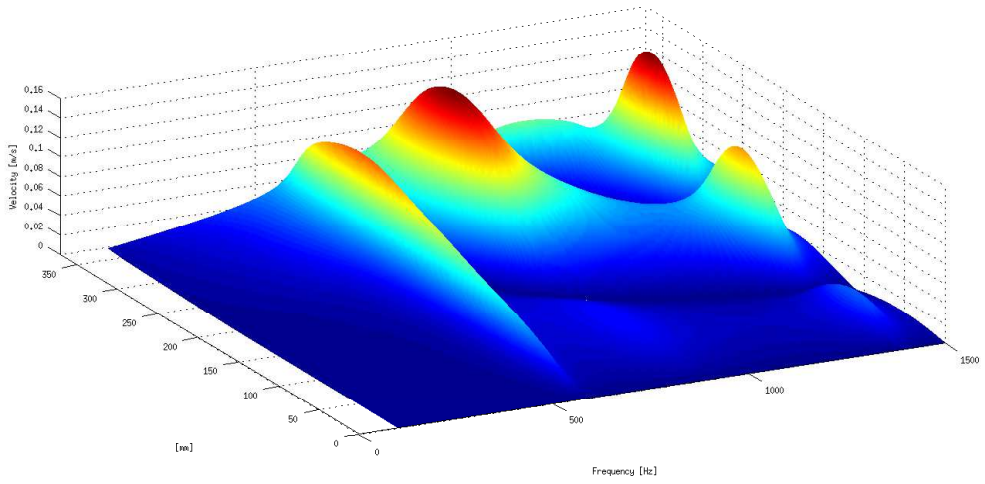

Figure 17: Velocity amplitude distribution along the spatial coordinate versus frequency.

r_{min} [mm]	r_{max} [mm]	f_{min} [Hz]	f_{max} [Hz]	f_{res} [Hz]	$\lvert\hat{p}'_{f_{res}}\rvert$ [Pa]
2	25	1	10000	672	4506
5	25	1	10000	574	2749
5	25	580	1000	580	2734
5	25	590	1000	590	2698
5	25	1	560	560	2726
5	25	1	550	550	2711
5	25	1	540	540	2694
5	25	1	530	530	2675
5	25	1	520	520	2654
5	25	1	510	510	2628

Table 7: Results of the optimization procedure obtained with different settings of the parameter constraints.

9.2 EXPERIMENTAL VALIDATION

The optimized resonator described above was manufactured[4] and measurements performed on the resonator were compared with theory. Fig. 18 shows a comparison between the calculated and measured acoustic pressure amplitude frequency characteristic of the optimized resonator. The agreement between theory and measurement is quite good, however the measured resonance frequency at the driving amplitude $|U_{in}| = 1\,\mathrm{V}$ is only $f_{r\,meas} = 551\,\mathrm{Hz}$ which is slightly less than calculated $f_{r\,calc} = 574\,\mathrm{Hz}$ (4 % difference). This discrepancy could probably be attributed to the differences between the mathematical description of the optimized resonator and the actual shape of the manufactured resonator. The frequencies in Figure 18 were normalized to the individual resonance frequencies $\Omega' = f/f_{r_{res}}$ for easier visual comparison. Also worth noting is that the resonance frequency of the system shifts downward with increasing input voltage amplitude ($f_{r\,meas} = 549\,\mathrm{Hz}$ with $|U_{in}| = 15\,\mathrm{V}$). This softening-spring-like behaviour is also predicted in the calculated characteristic.

Fig. 19 shows computed and measured acoustic pressure amplitudes versus the input voltage of the loudspeaker-resonator system with the optimized resonator. A very good agreement between theory and measurement can be observed. Also worth mentioning is that the calculation is valid even though non-linear generation of higher harmonics was not considered here. Dissipation in the boundary layer due to turbulence itself is able to capture the non-linear damping of the rising acoustic pressure. The calculated acoustic pressure amplitude versus input voltage characteristic without considering turbulence ($\tilde{\nu} = 1$) is also shown

4 Machined from two pieces of duralumin block which were then joined together.

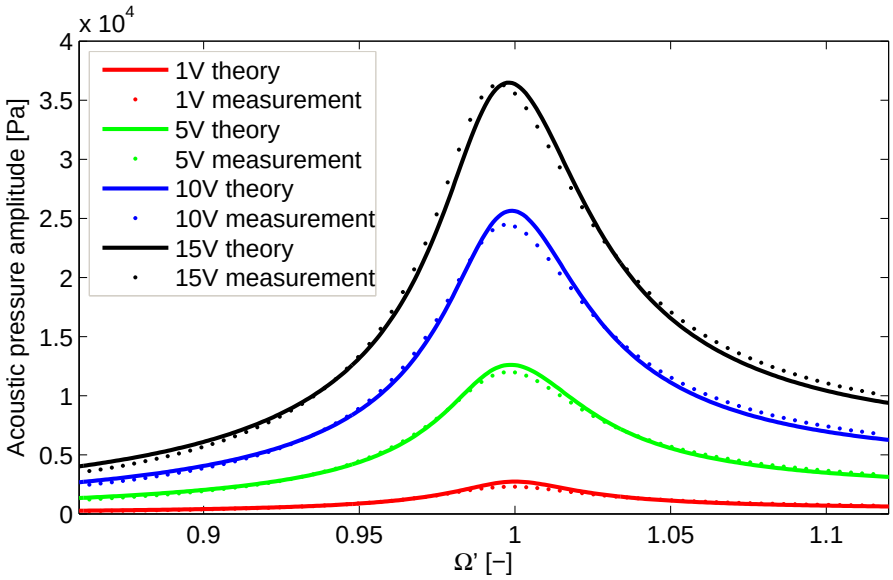

Figure 18: Measured and computed acoustic pressure amplitude frequency characteristics of the loudspeaker-resonator system with the optimized resonator.

for comparison. Fig. 20 shows time-course of an acoustic pressure in the resonator driven with a harmonic signal at the resonance frequency. Distortion of the waveform can be observed but a shock wave is not formed.

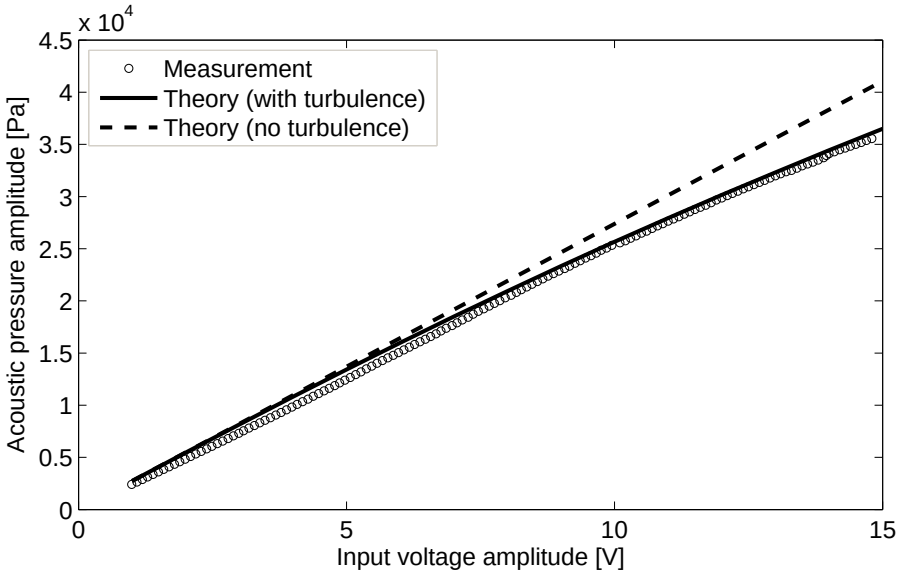

Figure 19: Measured and computed acoustic pressure amplitude versus input voltage of the loudspeaker-resonator system with the optimized resonator.

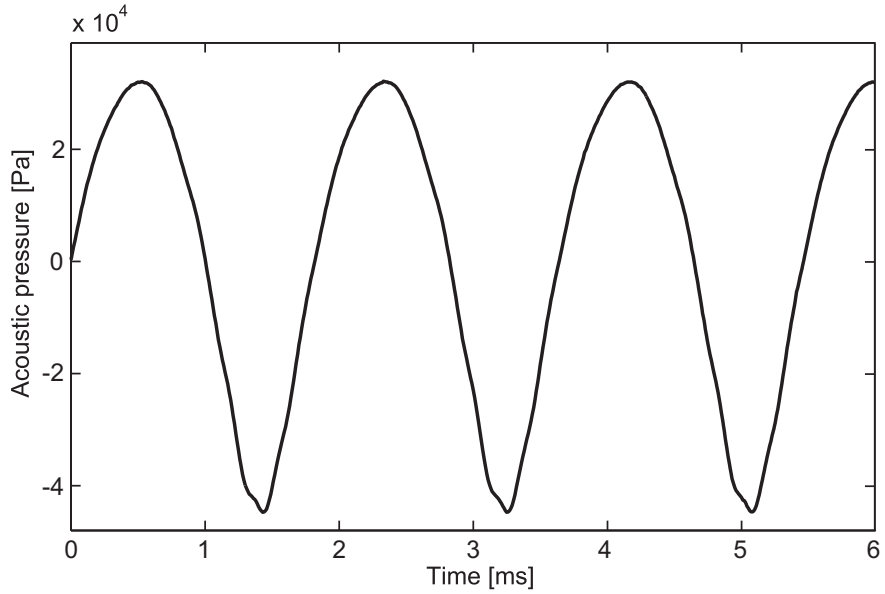

Figure 20: Acoustic pressure versus time measured in the optimized resonator driven at resonance ($f = 549\,\mathrm{Hz}$, $|U_{in}| = 15\,\mathrm{V}$).

10

SIMPLE ACOUSTIC COMPRESSOR

10.1 ACOUSTIC COMPRESSOR CONSTRUCTION

The loudspeaker-acoustic resonator system described in the previous chapter is utilized here to build a simple acoustic compressor.

The acoustic compressor was built by installing a suction port in the resonator wall where the standing wave has its pressure node (at $x = 272\,\text{mm}$ from the closed end of the resonator in our case) and a delivery port in the resonator wall where the standing wave has its anti-node (at $x = 0\,\text{mm}$).

With this arrangement alone, it is already possible to produce one-way air flow[1] [41], however the value of the air flow-rate obtained in this way is very small. For this reason the delivery port was fitted with a valve which rectifies the medium flow and therefore allows much higher values of air flow-rate to be achieved. In the experiments a reed-type passive valve has been used due to its simplicity and, more importantly, due to its ability to operate at high frequencies. The valve opens when an acoustic pressure inside the resonator cavity rises above the static ambient pressure at the opposite side of the reed and closes when the acoustic pressure falls bellow this static pressure level resulting in one-way air flow.

1 This is possible due to nonlinear properties of a fluid – with the rising acoustic pressure amplitude inside the resonator, some small dc component emerges at the pressure anti-node. This creates a static pressure gradient inside the resonator causing an air flow between the suction port and the delivery port.

A delivery port – a circular hole of 4 mm diameter with the center at the resonator axis of symmetry was drilled in the cap closing the resonator at its narrow end (at $x = 0$ mm). A delivery valve, enclosed inside a small metal box, was installed in a way shown in Figure 21. This box (the delivery valve housing) features two outlets for the connection of the pressure gauge and the air-flow meter. It also features a small glass window in its top wall, which can be used for the measurement of the reed displacement using a laser vibrometer. Two holes of 2 mm diameter drilled in the opposite sides of the resonator wall at the pressure node serve as suction ports.

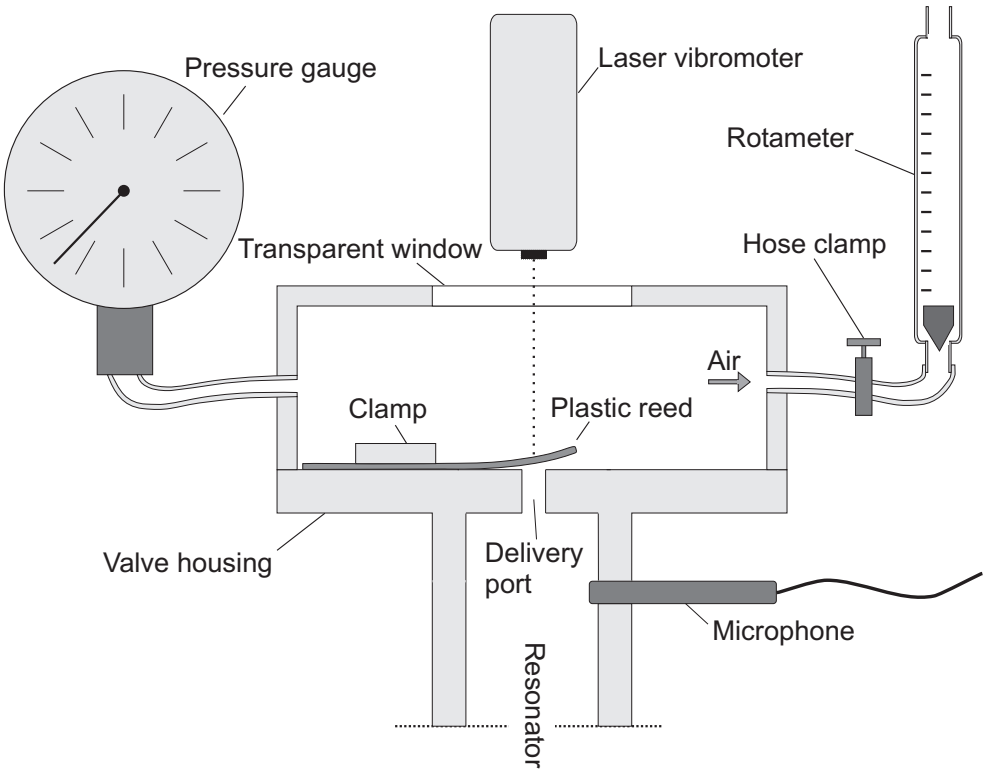

Figure 21: Valve housing configuration.

10.2 RESULTS

10.2.1 *Experimental setup*

All measurements were performed at room conditions using air as a compressed medium. Electrical signal driving the loudspeaker was generated with a computer using the LabVIEW environment and amplified with the Akiyama AMD400 amplifier. Acoustic pressure measurements were made in the LabVIEW environment using the NI PCI-6251 data acquisition card and the G.R.A.S. 12AA pre-amplifier with the G.R.A.S. 40DP 1/8" microphone which was attached from the side of the resonator as shown in Figure 21. Static pressure was measured using the PTL Prematlak 2010 pressure gauge, air volume flow-rate was measured using the Rheotest Medingen PG05 rotameter and the $\mu\epsilon$ optoNCDT ILD2300 laser vibrometer was used for the reed displacement measurement.

Fig. 22 shows a photograph of the experimental setup.

10.2.2 *Static pressure with no flow*

When an acoustic pressure is present inside the resonator, the delivery valve acts as a rectifier - increasing static pressure on the opposite side of the valve. By closing the hose clamp that controls the air flow (see Fig. 21), air is prevented from leaving the delivery valve housing resulting in the static pressure build-up. Since there is no air-flow out of the delivery valve housing, an optimally performing valve would eventually produce static pressure (pressure inside the delivery valve housing) equal to the acoustic pressure amplitude (inside the resonator). Displacement of the reed should decrease with the rising static pressure and the reed

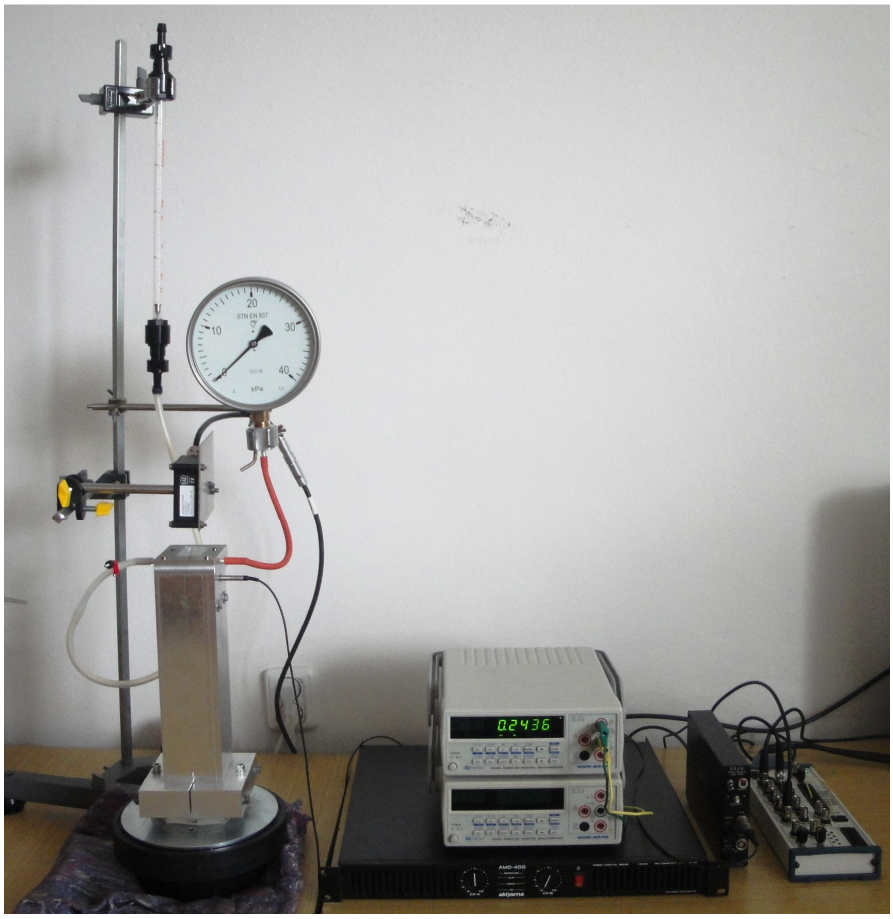

Figure 22: Acoustic compressor experimental setup. Selenium driver with the resonator attached to it is in the left part of the picture. Delivery valve housing is attached on the top of the resonator and laser vibrometer is placed above. Red hose connects the pressure gauge and white hose with a hose clamp leads to the flow-meter. Microphone is attached from the side of the resonator.

should eventually stop vibrating once the steady-state is reached – when the static pressure reaches the value of the acoustic pressure amplitude. This is not possible in our simple arrangement where the reed is not allowed to vibrate symmetrically but we can expect better performing reeds having smaller displacement.

A number of different valve reeds were tested and it was found that dimensions of reeds have a significant impact on their performance. In the following we present results for the four different reeds shown in Fig. 23. Each reed was made from a 130 μm thick PVC foil.

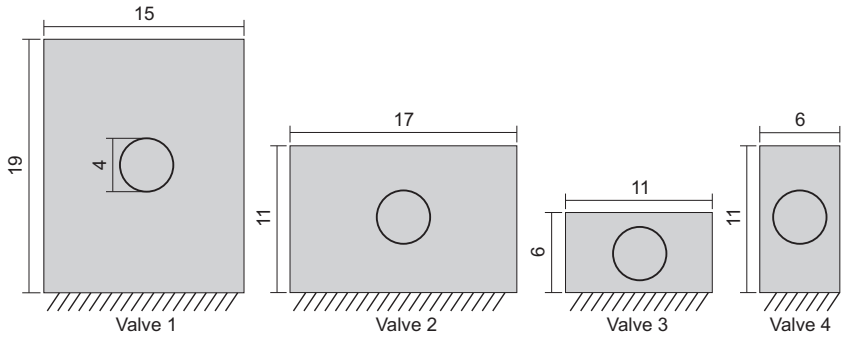

Figure 23: Valve reeds used in the experiment. Dimensions are in millimetres. Circles in the middle of each reed denote the position of the delivery port.

Fig. 24 shows measurement of the steady-state reed displacement versus time for the four different reeds shown in Fig. 23. The resonator was driven with a sine-wave signal at the resonance frequency $f_{res} = 551\,\mathrm{Hz}$ with the input voltage amplitude $|U_{in}| = 10\,\mathrm{V}$. It can be observed that the valve reed 1 tracks the acoustic pressure well. It opens for only short time interval during each cycle with the maximum displacement around 0.1 mm. On the other hand the valve reed 4 does not track the acoustic pressure very well. It is open during most of the cycle and its maximum displacement is roughly seven times bigger than the maximum displace-

ment of the valve reed 1. Valve reeds 2 and 3 behave somewhere between these two extremes.

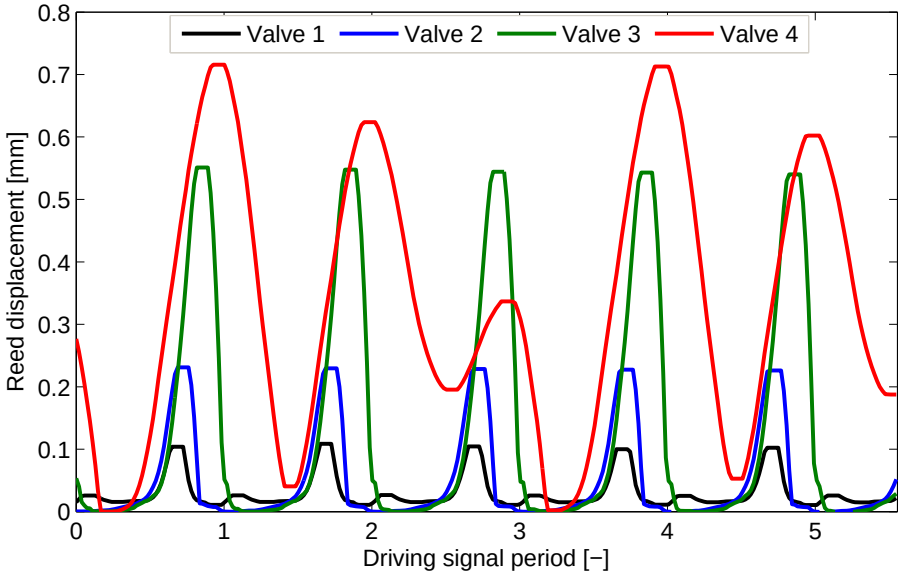

Figure 24: Displacement versus time characteristics for four different valve reeds shown in Fig. 23. Displacement was measured with the laser beam pointing at the center of the delivery port.

Static pressures inside the delivery valve housing measured at these conditions are summarized in Tab. 8.

It is clear that valve reeds which behave similarly to the ideal one – exhibiting a smaller displacement, which are able to track the acoustic pressure more accurately (i.e. respond faster) produce higher static pressures. Valve reed 1 will be used for all of the experiments described below.

Fig. 25 shows the valve displacement amplitude versus the input voltage amplitude characteristics. It can be observed that the valve reed displacement grows roughly proportionately with the input voltage suggesting a good - linear behaviour of the valve.

Reed number	1	2	3	4
Pressure [kPa]	20	16	7	0

Table 8: Static pressures measured inside of the delivery valve housing. The resonator was driven at resonance with input voltage amplitude $|U_{in}| = 10\,\mathrm{V}$.

Fig. 26 shows the measured static pressure and the acoustic pressure amplitudes versus the input voltage amplitude. It can be observed that the system possesses the desired characteristic - most of the acoustic pressure amplitude is rectified into the static pressure.

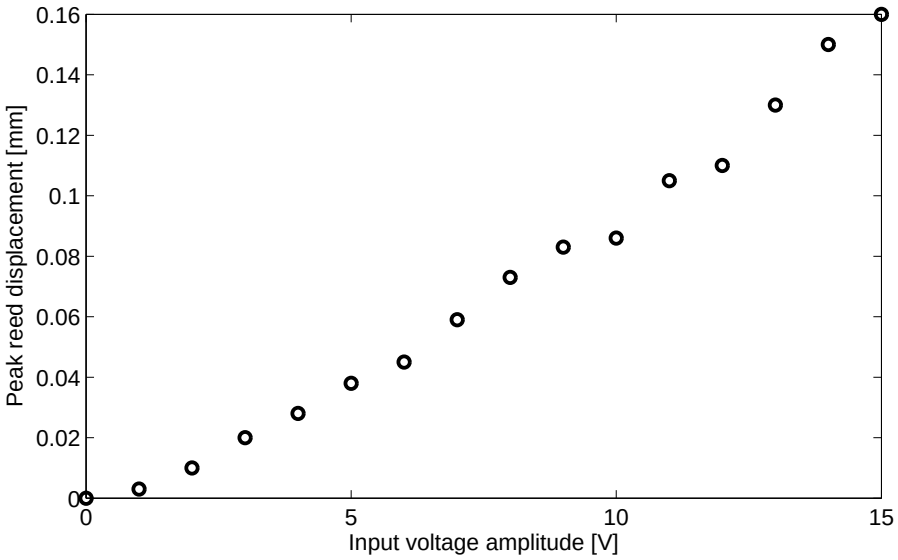

Figure 25: Valve reed 1 displacement amplitude versus the input voltage amplitude.

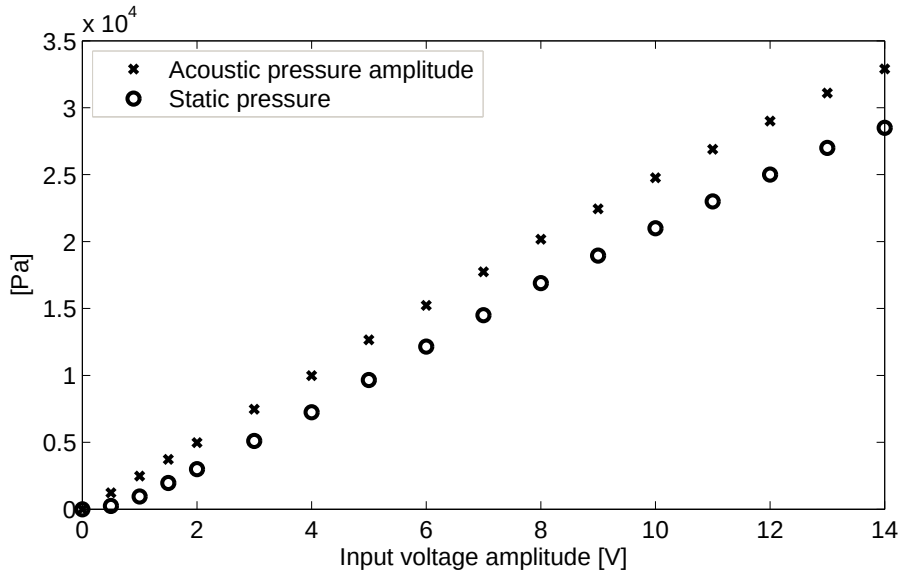

Figure 26: Acoustic pressure amplitude inside the resonator measured near the delivery port (as shown in Figure 21) and static pressure measured inside the delivery valve housing versus the input voltage amplitude.

10.2.3 *Resonator with air flow*

By gradually releasing the hose clamp, air is allowed to escape the valve housing resulting in the decrease of the static (delivery) pressure and one-way air flow through the resonator. Fig. 27 shows the air volume flow-rate versus the delivery pressure measured at three different input voltage amplitudes.

It was observed that the frequency at which the maximum air flow is achieved increases with opening of the hose clamp. However, it does not depend on the absolute value of the air flow rate or on the delivery pressure. Fig. 28 illustrates this frequency shift. The vertical axis represents frequency at which the air flow is maximal (for a given hose clamp setting) while the horizontal axis represents this air flow rate as a percentage of

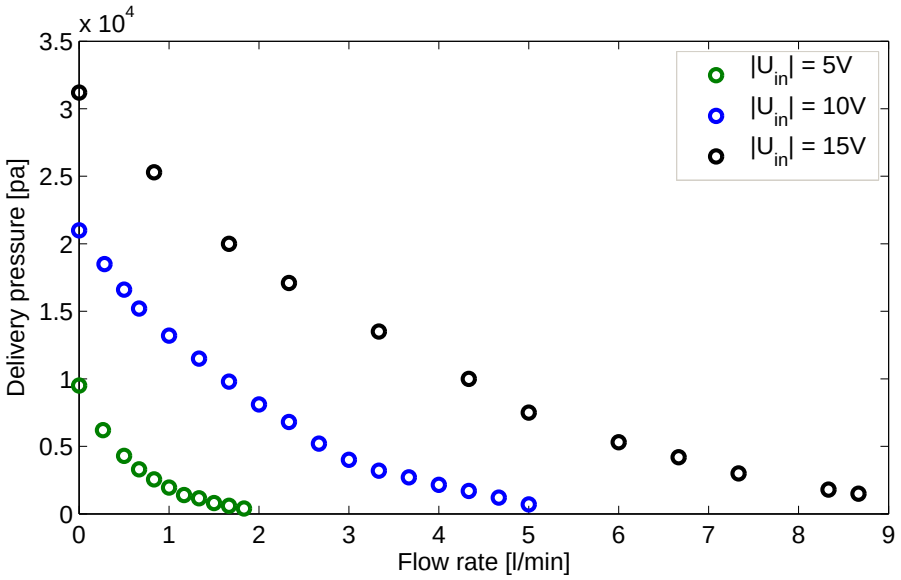

Figure 27: Air mass flow-rate versus delivery pressure measured for three different input voltage amplitudes.

the maximum possible air flow rate - with the hose clamp removed. This is measured for three different input voltage amplitudes. In other words, measured values represent how the air flow rate and the frequency at which the air flow rate is maximal changes with the opening of the hose clamp. It can be observed that the frequency shifts similarly (in relative terms) for all three input voltages - irrespective of the absolute air flow rate or the static pressure. It seems that the frequency at which air flow rate is maximal depends only on how much the hose clamp is opened. Possible explanation of this behaviour is that as the clamp is opened the effective geometry of the cavity behind the delivery valve changes. Since this cavity itself forms an acoustic system the change in its geometry could affect the function of the delivery valve. Similar behaviour was also observed by Masuda and Kawashima [42].

Measured frequency characteristic of the air volume flow-rate at the input voltage $|U_{in}| = 15\,\mathrm{V}$ with the hose clamp removed is shown in

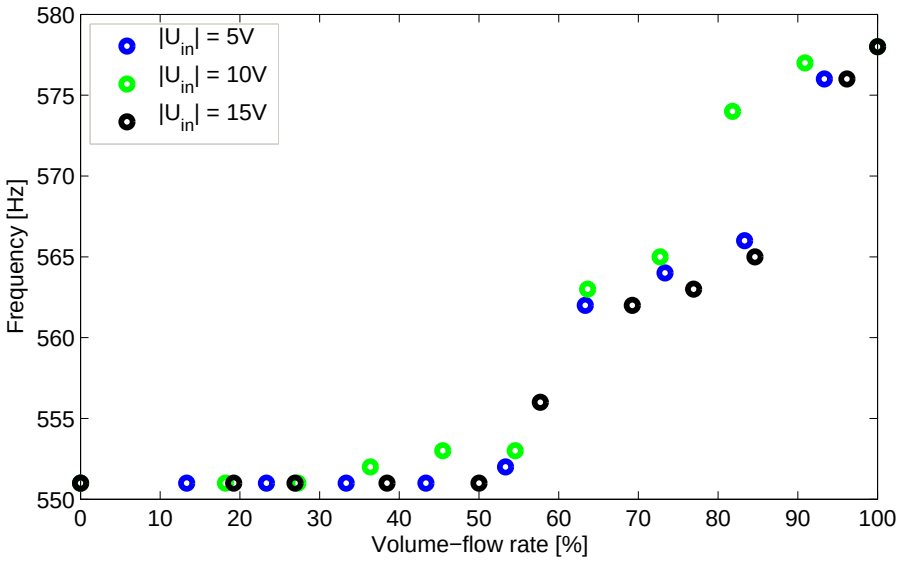

Figure 28: Shift of the driving signal frequency at which the air flow-rate is maximal as the hose clamp is opened. Description of the figure is given in the text above.

Fig. 29. It can be observed that under these conditions adjusting the driving frequency from the $f_{res} = 551\,\mathrm{Hz}$ to $f = 580\,\mathrm{Hz}$ results in roughly $14\,\%$ increase of the air volume flow-rate.

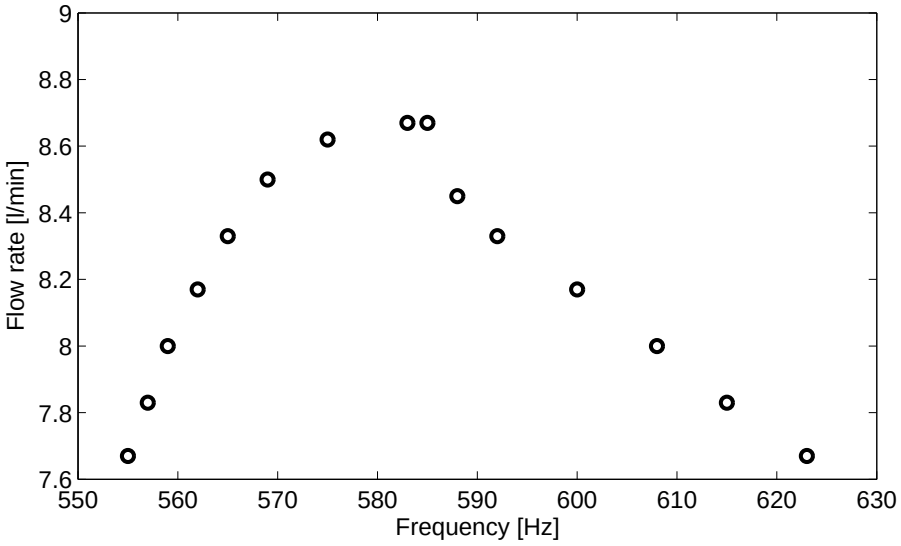

Figure 29: Frequency characteristic of the air volume flow-rate at input voltage $|U_{in}| = 15\,\mathrm{V}$ with the hose clamp removed.

Part III

CONCLUSIONS

11

CONCLUSIONS

11.1 SUMMARY

This thesis deals with the problem of generation, description and utilisation of high-amplitude acoustic fields in closed cavities. First a one dimensional, second-order partial differential model equation describing a sound field inside an axi-symmetrical variable-radius resonator is derived from basic fluid mechanics equations (Chapters 2 and 3). The model equation is then presented in the form suitable for numerical calculation (Chapter 4). Linearised model of the coupled loudspeaker-resonator acousto-mechanical system is described in the Chapter 5 and the model of energy losses in the boundary layer due to turbulence is presented in Chapter 6.

A new evolution algorithm-based method for optimization of acoustic-resonator shapes for generation of high-amplitude acoustic fields is presented in Chapter 7. The proposed method can be used to optimize shapes of resonators driven by a piston, shaker or a loudspeaker driver subject to a given set of constraints (resonance frequency constraints and geometrical constraints).

Numerical results (showed in Chapter 9) show that use of a properly optimized resonant cavity results in substantially stronger acoustic field compared with simple-shaped resonators of similar dimensions. A good agreement between the numerical results and the experimental data con-

firms the necessity of introduction of the model of energy dissipation in the boundary-layer due to turbulence in the governing equations.

Even if the optimization procedure cannot predict behaviour of strongly nonlinear acoustic fields, as it is based on a linear theory, it provides a systematic means of design of resonant cavities for high-amplitude acoustic applications such as e. g. thermoacoustic devices, plasma-chemical reactors or acoustical compressors. Utilizing the appropriately optimized resonant cavities together with commercially available loudspeakers could increase economic attractiveness of these promising applications.

The possibility of constructing a simple loudspeaker-driven acoustic resonator is demonstrated in Chapter 10. It has been shown that using the optimized resonator, construction of a acoustic compressor is possible even when using a relatively inexpensive and simple driving mechanism – a compression driver. Air volume flow-rates and delivery pressures we have been able to achieve (Fig. 27), are comparable or better than the ones reported by other authors ([16], [42] and [26]).

It was observed that dimensions of the reed, which acts as a delivery valve, has a significant impact on the performance of the compressor with better performing reeds exhibiting a smaller displacement and faster response.

11.2 ORIGINAL CONTRIBUTIONS

- A novel – Evolutionary algorithm-based optimization procedure which searches the space of possible axi-symmetrical resonator shapes defined by n control-points evenly distributed along the resonator axis of symmetry is presented. Resonator shape is given by the cubic spline interpolation of the n control-points. This is a major

difference compared with the previously used methods which considered only resonator shapes given by elementary functions. Moreover, the focus is on the optimization of the loudspeaker-acoustic resonator system which was not considered before at all. Algorithm is described in papers [58] and [55].

- A new optimization constraints-handling method which was not published before is presented in the thesis.

- Possibility of construction of a loudspeaker-driven acoustic compressor using the optimized resonator is demonstrated (experimental results were published in paper [57]).

11.3 RECOMMENDATIONS FOR FUTURE WORK

Further research could focus on improving the performance of the presented acoustic compressor. As the shape of the optimized resonator and the corresponding maximum acoustic pressure amplitude inside the resonator very much depend on the constraints used in the optimization procedure, by choosing different parameter constraints (especially the minimum radius r_{min}) optimization procedure would produce a different resonator shape, possibly yielding higher acoustic pressure amplitude. Acoustic compressor built using such a resonator is likely to have better performance than the one presented in the thesis.

The performance of the described acoustic compressor could possibly be further enhanced by using different (active) valve and by placing a suction port with a valve in the resonator wall where a standing wave has its pressure anti-node.

Part IV

APPENDIX

A

LOUDSPEAKER MODELLING

Cross-sectional view of the Selenium DT-405Ti compression driver is shown in Fig. 30.

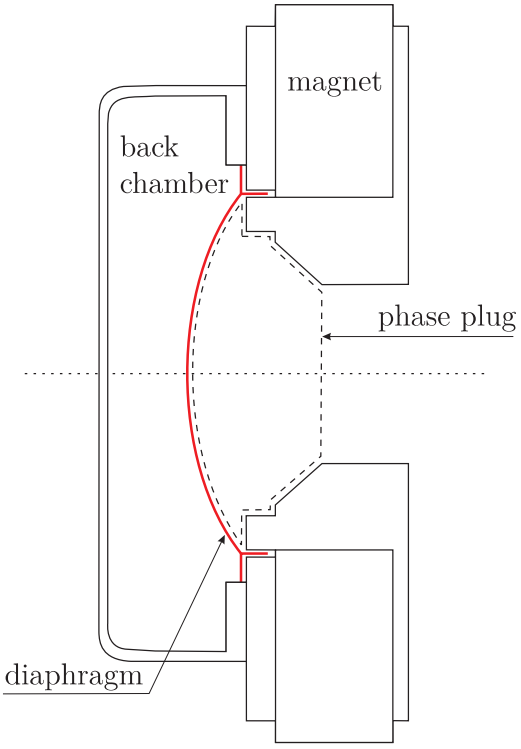

Figure 30: Cross–sectional view of the Selenium DT-405Ti compression driver.

INTERNAL WAVEGUIDE DESCRIPTION

Compression drivers utilize a phase plug which acts as an acoustic transformer providing better impedance match between the diaphragm and the waveguide throat. Phase plug is positioned in a close proximity to the diaphragm, creating a very narrow compression chamber. Sound waves have to travel through this narrow chamber and through the narrow slits in the phase plug. This however causes the air to behave non-linearly with increasing amplitude which is undesirable in our application. Moreover modelling of such a complex geometry becomes difficult, especially if non-linearities and damping in the boundary layer is to be taken into account. Since we intend to use the modelled loudspeaker to drive the resonator, impedance matching is not important for us and therefore the phase plug has been removed from the loudspeaker.

Looking at Fig. 30 it can be observed that what is left after phase plug removal is a waveguide of a complicated geometry that includes sudden contractions and cylindrical and conical sections. Moreover the diaphragm has a shape of a spherical cap (dome). For the purpose of modelling, this complex geometry had to be approximated. Fig. 31 shows actual and approximated geometry of the internal waveguide in front of the diaphragm.

Approximated geometry of the waveguide inside the loudspeaker is given by the formula

$$r(x) = \begin{cases} r_1 - x\dfrac{r_1 - r_2}{x1}, & 0 \leq x \leq x_1, \\ r_2 - (x - x_1)\dfrac{r_2 - r_3}{x_2}, & x_1 \leq x \leq x_1 + x_2, \\ r_3, & x_1 + x_2 \leq x \leq x_1 + x_2 + x_3, \end{cases}$$

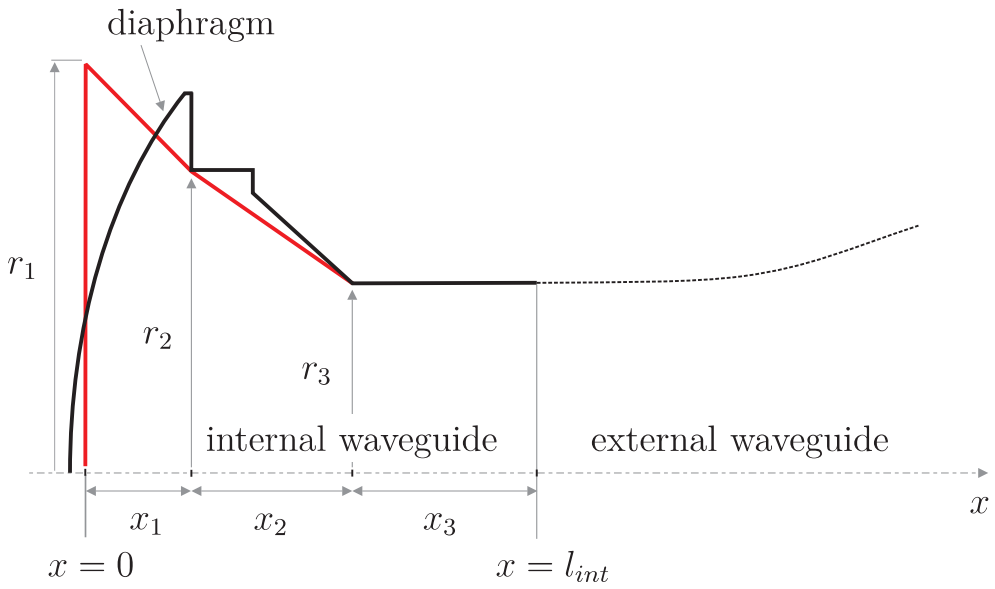

Figure 31: Actual (black color) and approximated (red color) shape of the waveguide inside the Selenium loudspeaker.

where x_2, x_3, r_2, r_3 were measured directly ($x_2 = 21\,\text{mm}$, $x_3 = 24\,\text{mm}$, $r_2 = 39.5\,\text{mm}$, $r_3 = 25\,\text{mm}$). r_1 is calculated from the area of the diaphragm; $r_1 = \sqrt{S_d/\pi} = 53.5\,\text{mm}$. Length of the first section of the internal waveguide $x_1 = 14\,\text{mm}$ was adjusted until good agreement between measured and computed frequency response of the loudspeaker-resonator acoustic system was achieved.

LOUDSPEAKER LINEAR PARAMETERS MEASUREMENT

Some of the unknown parameters in the lumped-element circuit (Fig. 2) can be determined directly by measurement (volume of the back chamber V, diaphragm area S_d) while others are determined indirectly by fitting measured loudspeaker characteristics with its model.

Assuming operation in vacuum we can eliminate acoustic quantities (acoustical radiation impedance Z_a tends to zero and c_a increases without bounds) and input electrical impedance can be expressed as

$$Z_{in} = R_v + \mathrm{i}\omega L_v + \frac{R_2 \mathrm{i}\omega L_2}{R_2 + \mathrm{i}\omega L_2} + \frac{1}{\frac{1}{R_{em}} + \mathrm{i}\omega C_{em} + \frac{1}{\mathrm{i}\omega L_{em}}} \tag{A.1}$$

where

$$R_{em} = \frac{(Bl)^2}{r_m}, \tag{A.2a}$$

$$C_{em} = \frac{m_m}{(Bl)^2}, \tag{A.2b}$$

$$L_{em} = c_m (Bl)^2 . \tag{A.2c}$$

R_{em} is the electrical resistance due to the mechanical losses, C_{em} is the electrical capacitance representing mechanical mass of the moving assembly and L_{em} is the electrical inductance representing the suspension compliance. All electrical parameters in Eq. (A.1) can be found by fitting the right hand side of this equation to the measured input electrical impedance of the loudspeaker in vacuum. Fig. 32 shows fitted and measured input impedance characteristic of the modelled loudspeaker in (near) vacuum (measurement was made in an airtight container from which the air was sucked-away until static pressure of around 2 kPa was achieved). Data were fitted in the least-square sense in MATLAB® software using its function *lsqcurvefit.m*. Electrical impedance was measured using impedance analyzer Agilent 4294A.

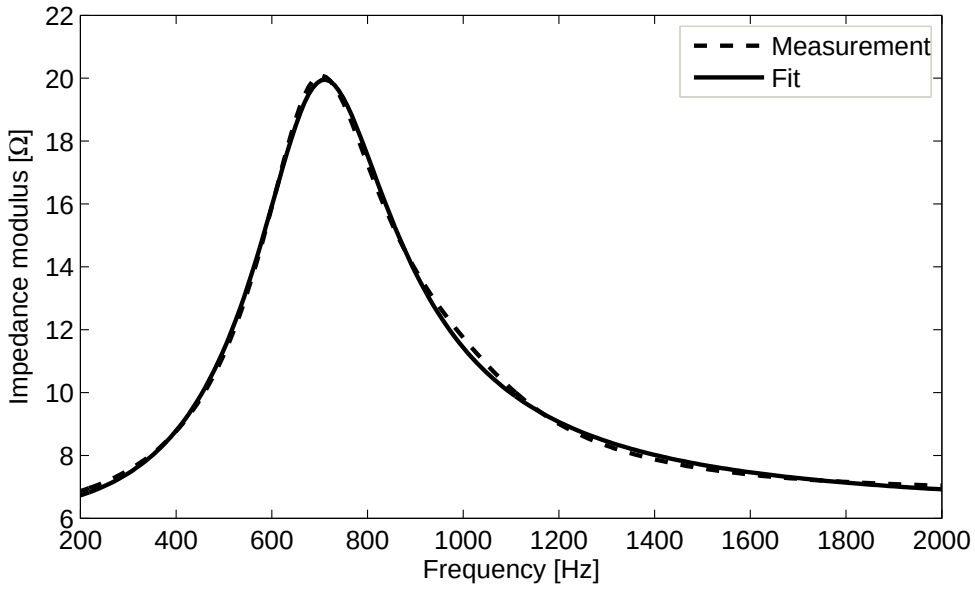

Figure 32: Modulus of input electrical impedance of a loudspeaker in an effective vacuum.

Bl-product and mechanical parameters estimation

Bl-product is usually determined using the added-mass or added-stiffness method [56]. These methods, however, are not easily exploitable for determining the *Bl*-product of a compression driver and might not give results accurate enough. Because of its accuracy a method based on non–contact measurement of the diaphragm displacement $\hat{y}$ using laser vibro-meter was chosen (see [32]).

Assuming $\hat{v} = \mathrm{i}\omega\hat{y}$ and eliminating acoustic quantities (vacuum) we can write (see Fig. 2)

$$\hat{y} = \frac{\hat{u}}{\mathrm{i}\omega Bl}\frac{Z_{em}}{Z_{in}}, \tag{A.3}$$

where

$$Z_{em} = \frac{1}{\frac{1}{R_{em}} + \mathrm{i}\omega C_{em} + \frac{1}{\mathrm{i}\omega L_{em}}} \tag{A.4}$$

and Z_{in} is given in Eq. (A.1). Since all electrical parameters have already been identified only unknown left is the Bl-product which is easily found by the means of least-squares fitting algorithm. Fig. 33 shows fitted and measured diaphragm displacement characteristic of the modelled loudspeaker.

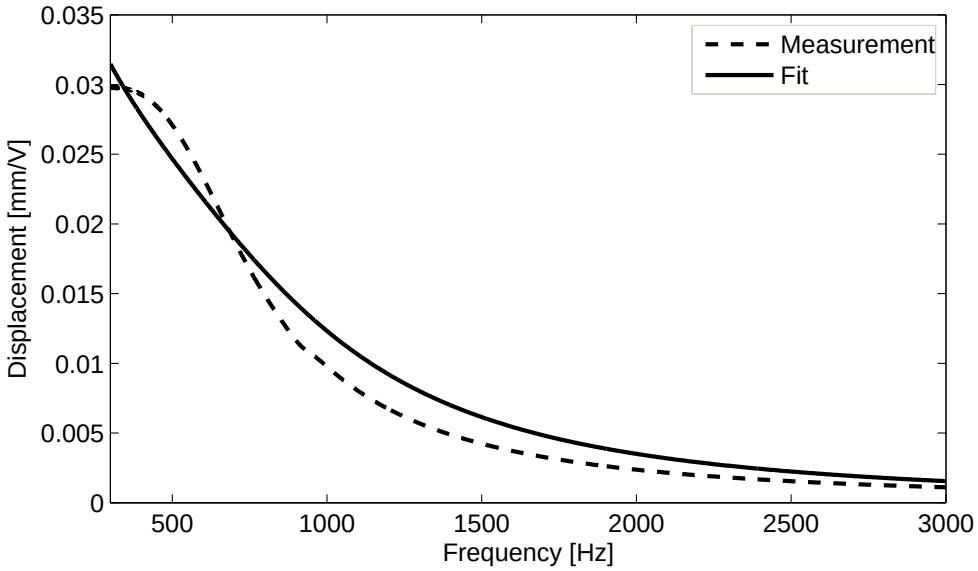

Figure 33: Diaphragm displacement characteristic of the modelled loudspeaker in an effective vacuum. Measurement was made using laser vibrometer Polytec Scanning Vibrometer PSV-400.

Mechanical parameters were then computed using Eq. (A.2). Linear parameters of the Selenium loudspeaker have thus been determined and are shown in Tab. 9.

R_v	$6.5\,\Omega$
L_v	$6.7 \times 10^{-5}\,\mathrm{H}$
r_m	$6.8\,\mathrm{kg\,s^{-1}}$
c_m	$1.2 \times 10^{-5}\,\mathrm{s^2 kg^{-1}}$
m_m	$4.1 \times 10^{-3}\,\mathrm{kg}$
V	$1.7 \times 10^{-4}\,\mathrm{m^3}$
c_a	$1.2 \times 10^{-9}\,\mathrm{m^4 kg^{-1} s^{-2}}$
S_d	$90 \times 10^{-4}\,\mathrm{m^2}$
Bl	$9.6\,\mathrm{T\,m}$

Table 9: Linear parameters of the Selenium D405Ti loudspeaker.

BIBLIOGRAPHY

[1] N. H. Asmar. *Partial Differential Equations and Boundary Value Problems*. Pearson Education, 2004. ISBN 9780131480964.

[2] T. Back and H. P. Schwefel. An overview of evolutionary algorithms for parameter optimisation. *Evolutionary Computation*, pages 1–23, 1993.

[3] T. Back, F. Hoffmeister, and H. P. Schwefel. Applications of evolutionary algorithms. report of the systems analysis research group (ls x1) sys-2/92. *University of Dortmund, Department of Computer Science*, 1992.

[4] M. Bednarik, M.; Cervenka. Propagation of nonlinear acoustic plane waves in an elastic gas-filled tube. *The Journal of the Acoustical Society of America*, 126, 07 2009.

[5] M. Bednarik, M.; Cervenka. Equations for description of nonlinear standing waves in constant-cross-sectioned resonators. *The Journal of the Acoustical Society of America*, 135, 03 2014. doi: 10.1121/1.4865262. URL `http://gen.lib.rus.ec/scimag/index.php?s=10.1121/1.4865262`.

[6] M. Bednarik, M.; Cervenka. Finite amplitude standing waves in resonators terminated by a general impedance. *The Journal of the Acoustical Society of America*, 137, 03 2015. doi: 10.1121/1.4908311.

[7] D. T. Blackstock. *Fundamentals of physical acoustics*. John Wiley & Sons, 2000. ISBN 978-0471319795.

[8] A. G. Bodine. Resonant gas compressor and method, January 8 1952. URL `http://www.google.com/patents/US2581902`. US Patent 2,581,902.

[9] M. Brdička, B. Sopko, and L. Samek. *Mechanika kontinua*. ACADEMIA, 2003. ISBN 978-80-200-2039-0.

[10] W. Chester. Resonant oscillations in closed tubes. *J. Fluid Mech.*, 18:44–64, 1964.

[11] W. Chester. Nonlinear resonant oscillations of a gas in a tube of varying cross-section. *Proc. R. Soc. Lond. A*, 444:591–604, 1994.

[12] Y. D. Chun and Y. H. Kim. Numerical analysis for nonlinear oscillations of gas in axisymmetric closed tubes. *JASA*, 108:2765–2774, 2000.

[13] D. A. Coley. *An Introduction to genetic algorithms for Scientists and Engineers*. World Scientific Publishing Co. Pte. Ltd., 1999. ISBN 981-02-3602-6.

[14] B Coppens and J. V. Sanders. Finite amplitude standing waves in rigid walled tubes. *JASA*, 52:1024–1034, 1968.

[15] D. B. Cruikshank. Experimental investigation of finite-amplitude acoustic oscillations in a closed tube. *JASA*, 52:1024–1036, 1972.

[16] A. El-Sabbagh. *Gas-filled Axisymmetric Acoustic Resonators*. VDM Verlag Dr. Muller Aktiengesellschaft & Co. KG, 2008. ISBN 978-3-639-09304-9.

[17] B. O. Enflo and C. M. Hedberg. *Theory of Nonlinear Acoustics in Fluids*. Springer, 2011. ISBN 978-9048159987.

[18] R. Erickson and B. Zinn. Modeling of finite amplitude acoustic waves in closed cavities using the galerkin method. *JASA*, 113:1863–1870, 2003.

[19] D. B. Fogel, A. J. Owens, and M. J. Wals. *Artificial Inteligence through Simulated Evolution*. John Wiley, 1966.

[20] D. F. Gaitan and A. A. Atchley. Finite amplitude standing waves in harmonic and anharmonic tubes. *JASA*, pages 2689–2495, 1993.

[21] H.; Lotton P.; Job S.; Bruneau M. Gusev, V. E.; Bailliet. Enhancement of the q of a nonlinear acoustic resonator by active suppression of harmonics. *The Journal of the Acoustical Society of America*, 103, 06 1998. doi: 10.1121/1.423090. URL `http://gen.lib.rus.ec/scimag/index.php?s=10.1121/1.423090`.

[22] Bailliet H., Lotton P., M. Bruneau, and V. Gusev. Coupling between electrodynamic loudspeakers and thermoacoustic cavities. *Acustica acta acustica*, 86:363–373, 2000.

[23] M. F. Hamilton, Y. A. Ilinskii, and E. A. Zabolotskaya. Linear and nonlinear frequency shifts in acoustical resonator with varying cross sections. *JASA*, 110:109–119, 2001.

[24] N. Hansen, S.P.N. Niederberger, L. Guzzella, and P. Koumoutsakos. A method for handling uncertainty in evolutionary optimization with an application to feedback control of combustion. *IEEE Transactions on Evolutionary Computation*, 13(1):180–197, 2009.

[25] J. H. Holland. *Adaptation in natural and artificial systems*. Bradford Books, 1992. ISBN 0-262-58111-6.

[26] A. Hossain, M. Kawahashi, T. Nagakita, M. Saito, and T. Fujioka. Application of finite amplitude oscillation of air-column in closed tube to design acoustic compressor. *Proceeding of 18th International Congress on Acoustics*, pages 381–384, 2004.

[27] X. Y. Huang, N. T. Nguyen, and Z. J. Jiao. Nonlinear standing waves in a resonator with feedback control. *JASA*, 122:38–41, 2007.

[28] M. Ilgamov, R. Zaripov, R. Galiullin, and V. Repin. Nonlinear oscillations of a gas in a tube. *Applied mechanics reviews*, 49:137–154, 1996.

[29] M. Ilgamov, R. Zaripov, R. Galiullin, and V. Repin. Nonlinear oscillations of a gas in a tube. *Applied Mechanics Reviews*, 49:137–154, 1996.

[30] Y. A. Ilinskii, B. Lipkens, T. S. Lucas, T. W. Van Doren, and E. A. Zabolotskaya. Nonlinear standing waves in an acoustical resonator. *JASA*, 104:2664–2674, November 1998.

[31] Y. A. Ilinskii, B. Lipkens, and E. A. Zabolotskaya. Energy losses in an acoustical resonator. *JASA*, 109:1859–1870, May 2001.

[32] W Klippel and U. Seidel. Fast and accurate measurement of linear transducer parameters. *Klippel GmbH, www.klippel.de*.

[33] O. Kramer. A review of constraint-handling techniques for evolution strategies. *Applied Computational Intelligence and Soft Computing*, page 11, 2000.

[34] O. Kramer. Evolutionary self-adaptation: a survey of operators and strategy parameters. *Evolutionary Intelligence*, pages 51–65, 2010.

[35] E. Kreyszig. *Advanced engineering mathematics*. WILEY INDIA PVT. LTD.-NEW DELHI, 2011. ISBN 9788126531356.

[36] L.D. Landau and E.M. Lifshits. *Fluid Mechanics, by L.D. Landau and E.M. Lifshitz*. Teoreticheskaiĭž aiž¡ fizika. Pergamon Press, 1959. URL `http://books.google.cz/books?id=CVbntgAACAAJ`.

[37] C. Lawrenson, B. Lipkens, T. S. Lucas, D. K. Perkins, Y. A. Van Doren, T. W. Ilinskii, B. Lipkens, T. S. Lucas, and T. W. Van Doren. Measurements of macrosonic standing waves in oscillating closed cavities. *JASA*, 104:623–636, 1998.

[38] X. Li, J. Finkbeiner, G. Raman, Ch. Daniels, and B. M Steinetz. Optimized shapes of oscillating resonators for generating high-amplitude pressure waves. *JASA*, 116:2814–2821, 2004.

[39] C. Luo, X. Y. Huang, and N. T. Nguyen. Effect of resonator dimmensions on nonlinear standing waves. *JASA*, 117:96–103, 2005.

[40] C. Luo, X. Y. Luang, and N. T. Nguyen. Generation of shock-free pressure waves in shaped resonators by boundary driving. *JASA*, 121:2515–2521, 2007.

[41] C. Macrosonix. Standing wave compressor, September 18 1991. URL `http://www.google.com/patents/EP0447134A2?cl=en`. EP Patent App. EP19,910,301,934.

[42] M. Masuda and S. Kawashima. A study on effects of the valves of acoustic compressors on their delivery flow rate. *International congress on acoustics Madrid*, september 2007.

[43] Q. Min, Q. Y. Zhang, J. J. Tian, Q. B. Wand, and W. Q. He. A study on the dissonant standing-wave tube with variable section and its extremely nonlinear standing-wave field. *Physics Letters A*, 377: 99–106, 2012.

[44] T Nakane. Discharge phenomenon in high-intensity acoustic standing wave field. *IEEE Trans. Plasma Sci.*

[45] W. Press, S. A. Teukolsky, W. T. Vetterling, and B. P. Flannery. *Numerical recepies*. Cambridge university press, 2007. ISBN 978-0-521-88068-8.

[46] O. V. Rudenko. Nonlinear standing waves, resonance phenomena, and frequency characteristics of distributed systems. *Acoustical Physics*, 55, 01 2009. doi: 10.1134/s1063771009010047. URL `http://gen.lib.rus.ec/scimag/index.php?s=10.1134/s1063771009010047`.

[47] O. V. Rudenko and S. I. Soluyan. *Theoretical foundations of nonlinear acoustics*. Springer-Verlag Publishing, 1977.

[48] H. P. Schwefel. *Numerical optimization of computer models*. Wiley, 1981. ISBN 0-471-09988-0.

[49] J.; Blumen A. Sokolov, I. M.; Klafter. Fractional kinetics. *Physics today*, 55, 11 2002. doi: 10.1063/1.1535007.

[50] M. Sugimoto, N.and Masuda, T Hashiguchi, and T. Doi. Frequency response of nonlinear oscillations of air column in a tube with an array of helmholtz resonators. *JASA*, 114:1772–1784, 2003.

[51] G. W. Swift. Thermoacoustic engines. *JASA*, 84:1145–1180, 1988.

[52] G. W. Swift. Thermoacoustic engines. *JASA*, 84:1145–1180, 1988.

[53] M. Červenka. *Nelinearní stojaté vlny v tekutinách.* PhD thesis, Czech technical university, 2003.

[54] M. Červenka and M. Bednařík. On the optimization of an acoustic resonator shape with respect to acoustic pressure amplitude. *Acust. Acta Acust.*, 99:183–191, 2013.

[55] M. Červenka, M. Šoltés, and M. Bednařík. Optimal shaping of acoustic resonators for the generation of high-amplitude standing waves. *JASA*, 136:1003–1012, 2014.

[56] Z. Škvor. *Vibrating Systems and their Equivalent Circuits.* Academia, 1991. ISBN 80-200-0035-6.

[57] M. Šoltés and M. Červenka. Acoustic compressor driven by horn loudspeaker. In *Proceedings of Forum Acusticum 2011*, pages 2837–2840. Madrid: European Acoustics Association, 2011. ISBN 978-84-694-1520-7.

[58] M. Šoltés and M. Červenka. Optimization of resonator shape in a coupled loudspeaker-resonator acoustic system. In *Euronoise Prague 2012 Proceedings*, pages 572–576. Prague: Czech Acoustic Society, 2012. ISBN 978-80-01-05013-2.

[59] X. Yao and Y. Liu. Evolutionary programming made faster. *IEEE Transactions on evolutionary computation*, pages 82–102, 1999.